PCCP

Simultaneous DNP Enhancements of ^{1}H and ^{13}C nuclei: theory and experiments

Journal:	*Physical Chemistry Chemical Physics*
Manuscript ID:	CP-ART-01-2015-000406.R1
Article Type:	Paper
Date Submitted by the Author:	23-Mar-2015
Complete List of Authors:	Shimon, Daphna; Weizmann Institute of Science, Chemical Physics Hovav, Yonatan; Weizmann Institute of Science, Chemical Physics Kaminker, Ilia; Weizmann Institute of Science, Chemical Physics Feintuch, Akiva; Weizmann Institute of Science, Chemical Physics Goldfarb, Daniella; Weizmann Institute of Science, Chemical Physics Department Vega, Shimon; Weizmann Institute of Science, Department of Chemical Physics

Simultaneous DNP Enhancements of ^{1}H and ^{13}C nuclei: theory and experiments

Daphna Shimon, Yonatan Hovav, Ilia Kaminker, Akiva Feintuch, Daniella Goldfarb, Shimon Vega

Abstract

DNP on heteronuclear spin systems often results in interesting phenomenon such as the polarization enhancement of one nucleus during MW irradiation at the "forbidden" transition frequencies of another nucleus or the polarization transfer between the nuclei without MW irradiation. In this work we discuss the spin dynamics in a four-spin model system of the form $\{e_a - e_b - (^1\mathrm{H},^{13}\mathrm{C})\}$, with Larmor frequencies ω_e, ω_H and ω_C, by performing Liouville space simulations. This spin system exhibits the common ^{1}H Solid Effect (SE), ^{13}C Cross Effect (CE) and in addition high order CE-DNP enhancements. Here we show, in particular, the "proton shifted ^{13}C-CE" mechanism that results in ^{13}C polarization when the model system, at one of its ^{13}C-CE conditions, is excited by a MW field at the zero quantum or double quantum electron-proton transitions $\omega_{MW} = \omega_a \pm \omega_H$ and $\omega_{MW} = \omega_b \pm \omega_H$. Further more, we introduce the "heteronuclear" CE mechanism that becomes efficient when the system is at one of its combined CE conditions $|\omega_a - \omega_b| = |\omega_H \pm \omega_C|$. At these conditions, simulations of the four-spin system show polarization transfer processes between the nuclei, during and without MW irradiation, resembling the polarization exchange effects often discussed in the literature.

To link the "microscopic" four-spin simulations to the experimental results we use the DNP lineshape simulations based on "macroscopic" rate equations describing the electron and nuclear polarization dynamics in large spin systems. This approach is applied based on electron-electron double resonance (ELDOR) measurements that show strong ^{1}H-SE features outside the EPR frequency range. Simulated ELDOR spectra combined with the *indirect* ^{13}C-CE (iCE) mechanism, result in additional proton shifted ^{13}C-DNP features that are similar to the experimental ones. These features are also observed experimentally in ^{13}C-DNP spectra of a sample containing 15 mM trityl in a glass forming solution of ^{13}C-glycerol/H_2O and are analyzed by calculating the basic ^{13}C-SE and ^{13}C-iCE shapes using simulated ELDOR spectra that were fitted to the experimental ones.

1 Introduction

During dynamic nuclear polarization (DNP) experiments NMR signals are enhanced by MW excitation of free electrons added to the samples of interest. In non-conducting solids, several DNP mechanisms are used to describe these enhancements. We can make a distinction between five mechanisms:

(i) The Solid Effect (SE) - where one electron e polarizes its neighboring nuclei by an effective MW irradiation on the "forbidden" zero quantum (ZQ_{en}) or double quantum (DQ_{en}) transitions, resulting in a positive and negative enhancement at the sum or difference frequencies of the electron and nuclear Larmor frequencies, $\omega_e \pm \omega_n$, respectively [1, 2, 3, 4, 5, 6, 7, 8, 9].

(ii) The *direct* Cross Effect (dCE) - where two dipolar-coupled electrons, e_a at a frequency ω_a and e_b at a frequency ω_b, polarize their neighboring nuclei via an on-resonance MW irradiation when the CE condition, $|\omega_a - \omega_b| \approx \omega_n$, is fulfilled [10, 11, 12, 13, 14, 15, 16]. At the CE condition there is full state-mixing between two degenerate energy levels such that on-resonance MW irradiation on the single quantum of electron e_a (SQ_a), for example, is also MW irradiation on the DQ_{bn} or ZQ_{bn} of electron e_b and the nucleus, and vice versa. The irradiation on these transitions results in enhancement of the nucleus, which, at the steady state, is proportional to the polarization difference between the two electrons, becomes equal to [17]:

$$P_n = \frac{P_a - P_b}{1 - P_a P_b} \tag{1}$$

where $\omega_a > \omega_b$.

(iii) The *indirect* Cross Effect (iCE) - where the same two dipolar-coupled electrons, at the CE condition, are not directly irradiated on but still polarize their neighboring nuclei. The two electrons are depolarized via a combination of off-resonance MW irradiation together with an electron spectral diffusion (eSD) process [17], and this together with other relaxation pathways creates a polarization difference, $P_a \neq P_b$, which results in polarization of a hyperfine coupled nucleus according to Eq. 1 [17]. The distinction between the dCE and iCE mechanisms is a consequence of possible differences in their enhancement dynamics due to differences in the relaxation processes and effective irradiation strengths in both cases. Ignoring this difference would mean that the dCE is included into the iCE process.

(iv) Thermal Mixing (TM) - which is a thermodynamic model that describes the nuclear enhancement in systems containing many coupled electrons and nuclei [2, 8, 18, 19, 20, 21, 22, 23]. It relies on reducing the spin temperature of the nuclear-Zeeman spin bath by the contact to the cold electron spin baths in the electron rotating frame [8, 19, 18, 24]. This process is active, in particular, when the nuclear Larmor frequencies are smaller than the EPR linewidth of the coupled electrons in the system, but was also used to explain the enhancement of nuclei with larger Larmor frequencies.

(v) the Overhauser Effect (OE) - where differentiation between ZQ and DQ electron-nuclear cross-relaxation mechanisms causes nuclear polarization [25, 26, 27, 28, 29]. This mechanism is responsible for DNP enhancements in solutions and conducting solids containing free radicals

[30, 31, 32, 33] and was recently shown to exist as well in MAS of dialectric solids [29].

Presently, DNP applications focus on ^{1}H and ^{13}C nuclei [10, 34, 35] though, many other nuclei have also been enhanced [34, 36, 37, 38, 39, 40, 41, 42, 43, 44, 45]. Different types of stable radicals are used; in particular nitroxide radicals with broad EPR spectra for ^{1}H-DNP (for example, TEMPO, TOTAPOL, bTbK and AMUPol [10, 46, 47, 48, 49, 50]) and narrow EPR spectrum radicals such as trityl [51] and BDPA [52, 53] for ^{13}C-DNP [54] and ^{2}H-DNP. When the nuclear Larmor frequencies are smaller than the EPR linewidths, mainly CE of TM enhancement is expected [10, 46, 47, 48, 49, 50], while in the case of larger Larmor frequencies the SE is responsible for the enhancement [2].

Samples containing radicals with broad EPR spectra that can simultaneously polarize several types of nuclei (with Larmor frequencies narrower than the EPR spectral width) generally show two DNP features: (i) The MW frequency swept DNP spectra of different nuclei are similar [2, 19, 20, 37, 38, 39, 40, 41, 56, 57], and (ii) there exists a polarization exchange between the different nuclei even without MW irradiation [37, 38]. These two features are described in the literature using the TM formalism. This formalism predicts that all nuclei in the sample reach the same nuclear spin temperature, which also means that their enhancements at each MW frequency are equal and thus their DNP spectra become the same [2, 24, 36].

The DNP spectra obtained with narrow-line radicals, sometimes exhibit enhancements of low gamma nuclei for MW irradiation frequencies outside the EPR spectrum. These positive and negative enhancements were not explained by the DNP mechanisms mentioned above. Such additional features in the DNP spectrum were first recorded by W. de Boer in ^{2}H-DNP spectra of a sample of m-xylene-d_6 doped with BDPA [36], in which positive and negative spectral features separated by $2\omega_D$ appeared on either side of the EPR line at $\omega_{MW} = \omega_e + \omega_H \pm \omega_D$ and $\omega_{MW} = \omega_e - \omega_H \pm \omega_D$, where ω_H and ω_D are the Larmor frequencies of ^{1}H and ^{2}H, respectively, and ω_e is the center of the EPR line. These were attributed to the "double solid-state effect" (double-SE), involving simultaneous spin flips of the electrons, protons and deuterons [36, 37]. Similar double-SE and double-SE-like spectral features were later reported in the literature, though in some of these cases their frequencies did not exactly fit the double SE case and an explanation for their appearance could not be found [41, 45, 58, 59]. In the present paper we present ^{13}C-DNP experiments on samples containing trityl radicals that also result in DNP spectra with extra spectral features outside of the EPR frequency range and that differ from de Boer's double-SE features because the frequency difference between the positive and negative enhancements is ω_C and not $2\omega_C$. We will account for these extra features theoretically.

Before presenting the trityl DNP data and the origin of their extra features, we discuss the the spin dynamics in a four-spin model system of the form $\{e_a - e_b - (^{1}\mathrm{H}, ^{13}\mathrm{C})\}$ by performing Liouville space simulations. This spin system exhibits the common ^{1}H-SE-DNP, ^{13}C-CE-DNP and high-order CE-DNP enhancements that can be correlated to the experimental observations. In particular, we show that irradiation on the ^{1}H ZQ and DQ transitions of each of the electrons in the pair at a ^{13}C-CE condition results in ^{13}C enhancements that appear at $\omega_{MW} = \omega_a \pm \omega_H$ and $\omega_{MW} = \omega_b \pm \omega_H$, resulting in a separation of ω_C between positive and negative enhancements.

These enhancements indicate the existence of a combined $\{^1$H-SE+^{13}C-CE$\}$ DNP mechanism. In this study we show the resemblance between these results and the actual results observed in our experiments.

Further calculations of the spin dynamics in the four-spin system $\{e_a - e_b - (^1\mathrm{H},^{13}\mathrm{C})\}$ show the existence of high-order "heteronuclear" CE mechanisms that corresponds to CE conditions of the form $|\omega_a - \omega_b| = |\omega_H \pm \omega_C|$. At these conditions the four-spin system simulations show possible polarization transfer processes between the nuclei, during MW irradiation and without it, that resembles the polarization exchange effects mentioned and discussed in Refs. [37, 38] in which, after saturation, one nucleus recovers its polarization due to the polarization of another nucleus. Conditions for these transfer process are investigated and their dynamic characteristics are derived. These findings will be verified experimentally in future studies of heteronuclear polarization transfer processes in TEMPOL samples.

To link the "microscopic" simulations to the experimental results we use the DNP lineshape simulations based on "macroscopic" rate equations describing the electron and nuclear polarization dynamics in large spin systems, recently introduced by Hovav et al. [17, 60]. There it was shown that the DNP enhancements in TEMPOL samples can be described by the iCE process after determining the electron polarization profile resulting from MW irradiation and eSD from two-dimensional electron-electron double resonance (2D-ELDOR) experiments [17]. This same approach is applied here after performing ELDOR measurements. These ELDOR spectra show strong ^{1}H-SE features outside the EPR spectrum frequency range that, combined with the ^{13}C-iCE mechanism, result in additional ^{13}C-DNP features that are similar to the experimental ones. In this study it is shown that the spin dynamics of the four-spin system at a $\{^1$H-SE+^{13}C-CE$\}$ type of DNP mechanism can be used to explain the additional spectral features observed in real samples.

2 Materials, experiments and simulations

2.1 Sample preparation

The experiments were performed on a sample containing 15 mM of trityl (Tris{8-carboxyl-2,2,6,6-tetra[2-(1-hydroxyethyl)]-benzo(1,2-d:4,5-d´)bis(1,3)dithiole-4-yl}methyl sodium salt) in a solution of 50/50 (% V/V) of $H_2O/1,3-^{13}C_2-$glycerol. $1,3-^{13}C_2-$glycerol was purchased from Cambridge Isotopes and trityl was purchased from Oxford Instruments. $30\mu l$ of the solution was placed in a glass vial, flash frozen with liquid nitrogen and then sealed with a flame. When mentioned, sonication was preformed in a bath sonicator for 10 minutes prior to freezing.

2.2 The spectrometer

All experiments were carried out in a hybrid pulsed-EPR-NMR spectrometer [61] at a magnetic field of 3.4 T, which corresponds to a ^{1}H-Larmor frequency of 144 MHz and an electron-Larmor frequency of approximately 95 GHz. Synchronization between the EPR and NMR

part of the spectrometer is possible and enables application of independent and simultaneous RF and MW irradiation pulse schemes. Two MW channels are installed and can be operated independently. A liquid helium flow cryostat positioned inside the magnet enables experiments in the temperature range of 2.5 K - 80 K.

2.3 EPR measurements

All EPR signals were detected using an echo detection scheme (α-τ-α-τ-echo) composed of two 400 nsec MW pulses ($\alpha \approx 90^0$) and an echo delay time of τ =600 nsec. In all cases the strength of the MW irradiation was approximately $\omega_1 \approx 600$ kHz as measured from electron nutation experiments (not shown). Integrated echo intensities were recorded for all EPR experiments using boxcar integration.

Electron spin-lattice relaxation times, T_{1e}, were measured at $\omega_{MW} = 94.866$ GHz by saturation-recovery experiments with an initial MW saturation pulse of 50 msec. Fitting of the data to extract T_{1e} values was done as described in Ref. [50].

ELDOR experiments (t_{MW}-t_d-α-τ-α-τ-echo) were conducted by varying the frequency of the excitation pulse, ω_{excite}, over a range of 400 MHz around the EPR spectrum. At each frequency, the excitation was $t_{MW} = 1$ sec long and was then followed by EPR echo detection at a frequency ω_{detect} using a second MW channel. Before each experiment, the ^{1}H nuclei were saturated using a train of saturation pulses (as described below), in order to mimic the DNP spectrum measurements. The repetition time in these experiments was set to 3 sec. Several ELDOR curves were measured by placing ω_{detect} at 5 different frequencies across the EPR spectrum. In the ELDOR case detection pulses of 450 nsec were used, with τ =1 μsec and t_d = 1 msec.

The echo detected (ED) EPR lineshapes were measured on a W-band spectrometer [62] at 10 K using pulses of $\frac{\pi}{2}$= 30 nsec, π = 60 nsec and an echo delay time of τ = 550 nsec, with a repetition time of 500 msec.

2.4 NMR measurements

The ^{13}C-NMR signals were detected using a free induction decay (FID) detection after a $\pi/2$ RF pulse of a length of 16 μs. Because of the low sensitivity of the ^{13}C signals in our setup the ^{13}C longitudinal relaxation times, T_{1C}, were determined by measuring the decay of the^{13}C signal after hyperpolarization by a MW irradiation at ω_{MW} = 94.84 GHz of t_{MW}=200 sec at 6.5 K or t_{MW} = 320 sec at 30 K. In all cases the resulting decay curves could be analyzed using a single exponent. Before each ^{13}C-NMR experiment the ^{13}C signal was saturated by applying a train of 100 alternating on-resonance x and y saturation pulses.

The ^{1}H-NMR signals were detected using a solid echo detection ($(\pi/2)_x - \tau - (\pi/2)_u$) with a $\pi/2$ pulse of a length of 3 μs and τ = 23 usec. The proton longitudinal relaxation times, T_{1H}, were measured by saturation recovery. In all cases the resulting curves could be analyzed using a single exponent. Before each ^{1}H-NMR experiment the ^{1}H signal was saturated by applying a

train of 20 alternating on-resonance x and y saturation pulses.

2.5 DNP measurements

Frequency swept DNP spectra were measured by applying MW irradiation of a length of t_{MW} = 320 sec at 6.5 K, $t_{MW} = 80$ sec at 10 K, or $t_{MW} = 900$ sec at 30 K, for ^{13}C-DNP, and of, t_{MW} = 40 sec at 6.5 K or $t_{MW} = 60$ sec at 30 K for ^{1}H-DNP, at a MW frequency ω_{excite} varying between 94.5 GHz and 95.06 GHz, followed by ^{13}C or ^{1}H signal detection.

DNP buildup curves were measured using continuous MW irradiation at frequency ω_{excite} = 94.83 GHz (the frequency of the maximum of the main DNP spectrum) or $\omega_{excite} = 94.7$ GHz (the frequency of the maximum of the outer pair of spectral features) and with a varying duration t_{MW} prior to either the ^{13}C or ^{1}H signal detection.

All the DNP experiments began with a train of saturation pulses as described above.

2.6 DNP simulations on model systems and macroscopic systems

Numerical simulations of the spin dynamics in small spin systems were performed by evaluating the time evolution of the matrix elements of the spin density operator assuming a main interaction Hamiltonian, H_0 with Zeeman, hyperfine and dipolar interaction terms, and a MW irradiation Hamiltonian, H_{MW}. The methods of simulation are described in detail in Refs. [9, 16, 63].

Calculations of the electron polarization distribution along the EPR spectrum during MW irradiation are based on the phenomenological rate equation model recently introduced by Hovav et al. for the simulation of the polarizations of the frequency bins composing this spectrum [60]. A summary of these calculations are presented later in the paper. The electron polarizations are used in order to calculate the basic lineshapes of the DNP spectra, which we then use to analyze the experimental DNP spectra. This is done as recently described by Hovav et al. [17].

3 DNP on model systems containing electrons and ^{13}C, ^{1}H nuclei

Before showing the experimental^{13}C-DNP data and their analysis, we first consider possible DNP polarization mechanisms that are present in small spin systems. Here we restrict ourselves to systems containing one or two electrons coupled to a ^{1}H and a ^{13}C nucleus. This discussion provides a basis for the understanding of some of the DNP phenomena involving nuclei with different gyromagnetic ratios, reported in the literature and also described in the experimental part of this publication. In the following we present a summary of all DNP effects that can be expected in these three-spin and four-spin model systems.

3.1 $\{^1\mathrm{H} - e - ^{13}\mathrm{C}\}$ model systems

3.1.1 Standard SE-DNP

The simplest DNP system containing ^{1}H and ^{13}C is the $\{^1\mathrm{H}-e-^{13}\mathrm{C}\}$ system, with one electron hyperfine coupled to both nuclei. The Hamiltonian of this system in the electron rotating frame of a MW field of intensity ω_1 applied at a frequency ω_{MW} has the form

$$H_0 = (\omega_e - \omega_{MW})S_z - \omega_H H_z - \omega_C C_z + d_{HC} H_z C_z \tag{2}$$
$$+A_{z,eH} S_z H_z + \frac{1}{2}(A^{\pm}_{eH} S_z H^+ + A^{\pm}_{eH} S_z H^-) + A_{z,eC} S_z C_z + \frac{1}{2}(A^{\pm}_{eC} S_z C^+ + A^{\pm}_{eC} S_z C^-_z)$$

where S_p are the electron angular momentum operators with $p = x, y, z$ and H_z, $H^{\pm}$,C_z and $C^{\pm}$ are the angular momentum operator components of ^{1}H and ^{13}C. $(\omega_e - \omega_{MW})$ is the electron off-resonance frequency, $A_{z,en}$ and $A^{\pm}_{en}$ are the secular and pseudo-secular coefficients of the dipolar-hyperfine interactions between the electron e and nucleus $n =^1$ H,^{13}C, and d_{HC} is the $^1\mathrm{H} -^{13}$ C heteronuclear dipolar interaction coefficient. During MW irradiation we must add to H_0 a term of MW irradiation with a strength ω_1:

$$H_{MW} = \omega_1 S_x. \tag{3}$$

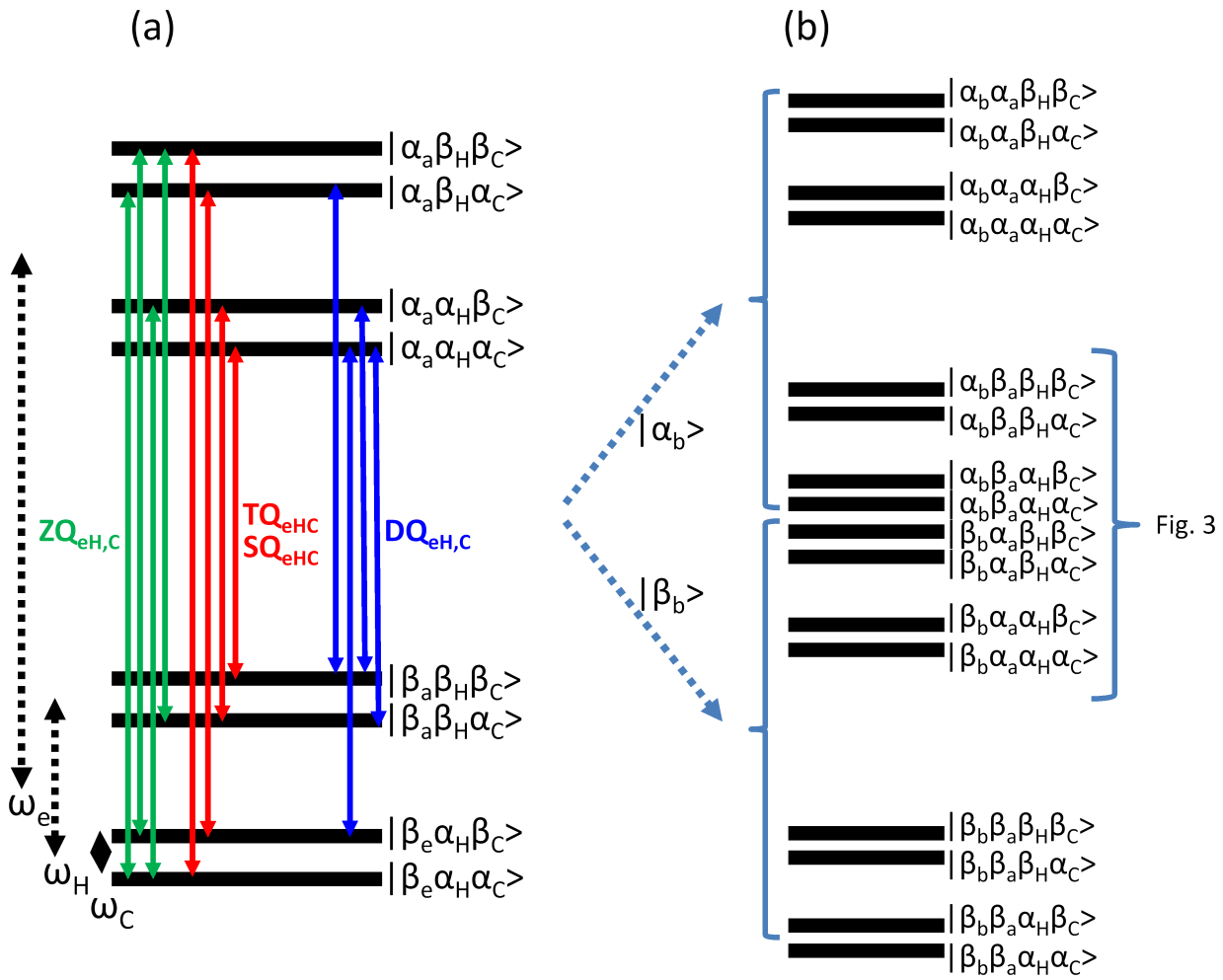

Figure 1: Energy level diagram of a (a) three spin system $\{^1\mathrm{H} - e - {}^{13}\mathrm{C}\}$ and of a (b) four spin system $\{e_a - e_b - (^1\mathrm{H}, {}^{13}\mathrm{C})\}$. (a) The DQ transitions of the electron with one of the nuclei are plotted in blue, the ZQ transitions of the electron with one of the nuclei are plotted in green, and the SQ and TQ transitions of all three spins are plotted in red. (b) The eight middle energy levels are plotted again in Fig. 3 as a function of the energy level difference between the electrons.

This Hamiltonian can be represented by an 8×8 matrix spanned by the spin states of the system with energies as shown in Fig. 1a. In this energy level diagram we can distinguish between electron single quantum (SQ_e) transitions ($\Delta m_e = \pm 1$), double quantum (DQ_{en}) and zero quantum (ZQ_{en}) transitions of the electron with ^{1}H or ^{13}C with $|\Delta m_e + \Delta m_n| = 2$ and $|\Delta m_e + \Delta m_n| = 0$, and combined single quantum, SQ_{eHC}, and triple quantum, TQ_{eHC}, transitions with $|\Delta m_e + \Delta m_{^{13}C} + \Delta m_{^1H}|$ equal to 1 and 3. Irradiation on one of the DQ_{en} and ZQ_{en} transitions at frequencies $\omega_{MW} = \omega_e \pm \omega_n$ will cause the standard positive and negative SE-DNP enhancement of the n nucleus. This is plotted in Fig. 2, with a scheme showing the different transitions below. The electron polarization is plotted in black, the ^{1}H polarization in magenta and the ^{13}C polarization in blue. The polarizations are normalized according to the thermal equilibrium polarization of the electron. The effective MW irradiation on the SE-DNP transitions is of strength $\omega^n_{1,eff} = \frac{A^{\pm}_{en}}{\omega_n}\omega_1$, derived from perturbation theory [9, 64] and the degree of enhancement is determined also by the electron and nuclear T_1's.

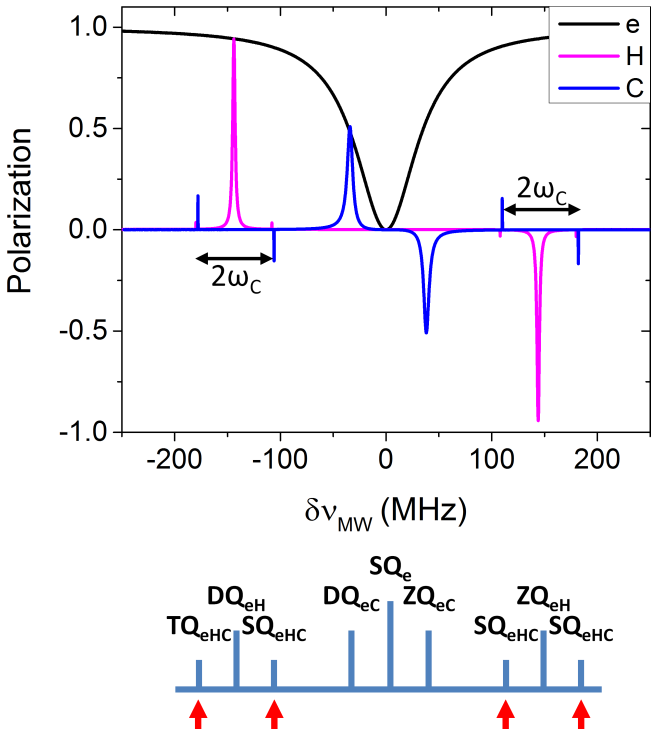

Figure 2: Simulated DNP spectra of the three spin system $\{^1\mathrm{H}-e-^{13}\mathrm{C}\}$. Plotted in the y-axis are the ^{1}H (magenta), ^{13}C (blue) and electron (black) polarizations with respect to the electron polarization at thermal equilibrium. The MW frequency scale is given with respect to $\nu_{ref} = 95 \cdot 10^3$ MHz: $\delta\nu_{MW} = \omega_{MW}/2\pi - \nu_{ref}$. At the bottom are plotted the transitions of the system. The red arrows mark the double-SE transitions: TQ_{eHC} and SQ_{eHC}. The parameters used to simulate the DNP spectra are: $T = 10$ K, $\omega_e = 95$ GHz, $\omega_H = 144$ MHz, $\omega_C = 36$ MHz, $A_{z,eH} = 0$ MHz, $A_{z,eC} = 0$ MHz, $A^{\pm}_{eH} = 0.5$ MHz, $A^{\pm}_{eC} = 0.125$ MHz, $d_{HC} = 0$ MHz, $\omega_1 = 0.5$ MHz, $T_{1e} = 100$ msec, $T_{1H} = 100$ sec, $T_{1C} = 500$ sec, $T_{2e} = 20$ usec, $T_{2n} = 100$ usec. The ^{13}C spectrum was shifted by 2 MHz in the x direction so it would not cover the ^{1}H polarization at the double-SE transitions.

3.1.2 Double-SE-DNP

Nuclear enhancements are also observed during irradiation at the four higher order SQ_{eHC} and TQ_{eHC} transitions. The frequencies of these transitions (see red arrows in Fig. 2) are $\omega_{MW} = \omega_e + \omega_H \pm \omega_C$ and $\omega_{MW} = \omega_e - \omega_H \pm \omega_C$ and the effective MW irradiation strength on these transitions is of the order of $\omega^{CH}_{1,eff} = \frac{A^{\pm}_{eH} A^{\pm}_{eC}}{\omega_H \omega_C}\omega_1$, also derived from perturbation theory [9, 64]. These weak irradiations can cause nuclear polarization via a high order SE-DNP process, named double-SE-DNP [36, 37], that results in narrow positive or negative lines in the DNP spectrum. When detecting ^{13}C signals, the double-SE induced enhancements appear at the MW frequencies given above, with positive and negative polarizations, separated by $2\omega_C$, around both the DQ_{eH} and the ZQ_{eH} transitions. During ^{1}H detection these enhancements appear at the same four frequencies but on the DQ_{eH} side they are both positive and on the ZQ_{eH} side they are both negative. In Fig. 2 the simulated frequency swept DNP spectra are shown for the three-spin system. All ^{13}C enhancement features mentioned here can be recognized (red arrows in Fig. 2) and the frequency width of the double-SE-polarizations are narrow as expected from

the weak $\omega_{1,eff}$.

The buildup characteristics of the four double-SE lines are determined by the strengths of the effective irradiation and the relaxation parameters of the system (listed in the figure caption).

In real samples these double-SE features appear outside of the EPR spectrum when $(\omega_H - \omega_C)$ exceeds the width of this spectrum. Thus for narrow-line radicals such as trityl the convolution of the EPR lineshape with delta functions appearing at the double-SE frequencies can reconstruct the DNP features that appear at both sides of the main DNP spectrum and that should show the expected $2\omega_C$ separation between their positive and negative enhancements. Because of the very low effective MW strength on the high order transitions the double-SE enhancements are weaker than the standard SE.

3.2 $\{e_a - e_b - (^1\mathrm{H}, ^{13}\mathrm{C})\}$ systems

3.2.1 Degenerate energy levels

The next system that we consider is one containing two interacting electrons coupled to ^{1}H and ^{13}C nuclei: $\{e_a - e_b - (^1\mathrm{H}, ^{13}\mathrm{C})\}$. The Hamiltonian of this system in the MW rotating frame is:

$$\begin{aligned} H_0 &= \omega_H H_z + \omega_C C_z + D_{ab}(3S_{z,a}S_{z,b} - \overline{S}_a \cdot \overline{S}_b) + d_{HC} H_z C_z \\ &+ \sum_{e=a,b} [(\omega_e - \omega_{MW})S_{z,e} + A_{z,eH} S_{z,e} H_z + \frac{1}{2}(A^{\pm}_{eH} S_{z,e} H^{+} + A^{\pm}_{eH} S_{z,e} H^{-}) \\ &+ A_{z,eC} S_z C_z + \frac{1}{2}(A^{\pm}_{eC} S_{z,e} C^{+} + A^{\pm}_{eC} S_{z,e} C^{-})] \end{aligned} \tag{4}$$

where D_{ab} is the electron-electron dipolar coupling constant. This system has 16 energy levels (see Fig. 1b) and we again recognize the SQ_e, DQ_{en} and ZQ_{en} transitions and the combined SQ_{eHC} and TQ_{eHC} transitions. In this four-spin system, the electron frequencies can satisfy the ^{13}C-CE-DNP conditions, $|\omega_a - \omega_b| \approx \omega_C$, the ^{1}H-CE-DNP conditions, $|\omega_a - \omega_b| \approx \omega_H$, and higher order CE conditions, as will be discussed below. We will not consider the case of two electrons with $\omega_a \approx \omega_b$, resulting in large mixing between the electrons.

A representation of the different possible CE conditions (i.e. energy level degeneracies) of the four-spin system is shown in Fig. 3a, where the 8 middle energy levels are drawn as a function of $(\omega_a - \omega_b)$. Each degeneracy corresponds to an overlap between two of the SQ, DQ, ZQ and TQ transitions as shown in Fig. 3b. We recognize 8 degeneracies: (2,2') and (4,4') the standard CE-DNP conditions of ^{1}H and ^{13}C, respectively, and higher order CE-DNP conditions, (1,1') where $|\omega_a - \omega_b| = \omega_H + \omega_C$ (and DQ_{aH} overlaps with ZQ_{bC} and ZQ_{aH} with DQ_{bC}), and (3,3') where $|\omega_a - \omega_b| = \omega_H - \omega_C$ (and DQ_{aH} overlaps with DQ_{bC} and ZQ_{aH} with ZQ_{bC}). The nature of these last two conditions and their effect on the DNP mechanisms will be discussed below, but first we will concentrate on the standard CE conditions.

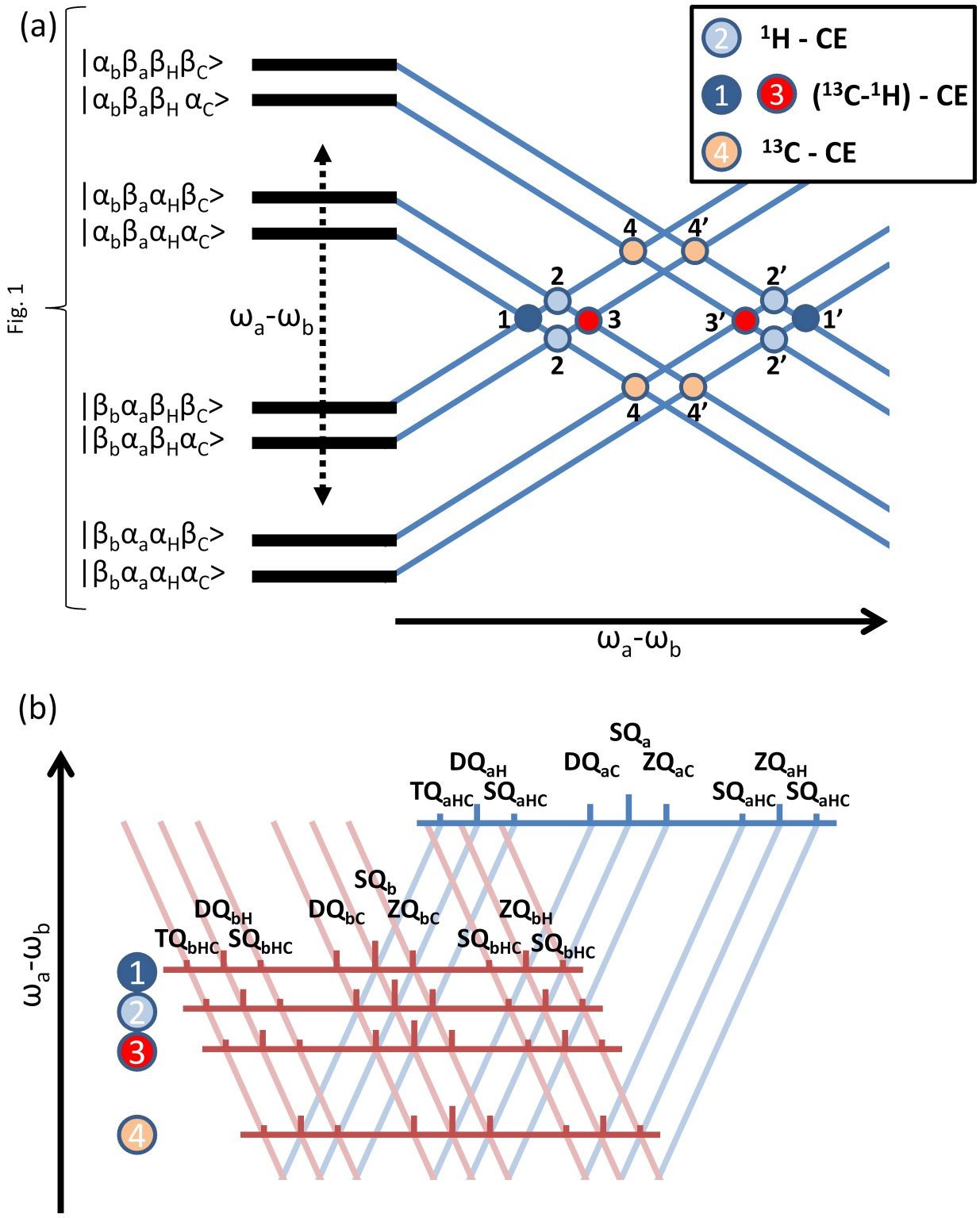

Figure 3: (a) A diagram of the eight middle energy levels of a four spin system, $\{e_a - e_b - (^1\mathrm{H}, ^{13}\mathrm{C})\}$, as a function of the frequency difference between the electrons, $\omega_a - \omega_b$, showing the different degeneracies possible in this system. The degeneracies correspond to regular ^{1}H-CE and ^{13}C-CE conditions and high order CE conditions, as listed in the figure legend. The full energy level diagram is plotted in Fig. 1. (b) Sketches of the transitions of electron a (in blue) and electron b (in red) as a function of the frequency difference between the electrons, $\omega_a - \omega_b$, showing the overlaps of the transitions at the different CE conditions.

3.2.2 The ^{13}C−CE conditions {4,4'}

The direct ^{13}C−CE:

At the CE condition (4), $(\omega_b - \omega_a) = \omega_C$, the SQ_a and ZQ_{bC} transitions overlap as well as the DQ_{aC} and SQ_b transitions as shown in Fig. 4 (blue arrows). The small splittings of the transitions are due to the electron-electron dipolar interaction. At this CE condition the $|\beta_a\alpha_b\alpha_H\beta_C>$ and $|\alpha_a\beta_b\alpha_H\alpha_C>$ states and the $|\beta_a\alpha_b\beta_H\beta_C>$ and $|\alpha_a\beta_b\beta_H\alpha_C>$ states have equal energies and mix because of small effective off diagonal matrix elements between them of magnitude $D_{ab}A^{\pm}_{eC}/\omega_C$, as described by degenerate perturbation theory [10, 16, 64, 65, 66]. MW irradiation at the SQ_a and SQ_b frequencies results in the standard ^{13}C-CE-DNP enhancements and irradiation at the non-overlapping ZQ_{aC} or DQ_{bC} frequencies results in reduced ^{13}C-SE-DNP enhancements (see Fig. 4). Similar enhancements are obtained for (4'), where $(\omega_b - \omega_a) = -\omega_C$. The energy level diagram of this system at CE condition (4) is shown in the SI.

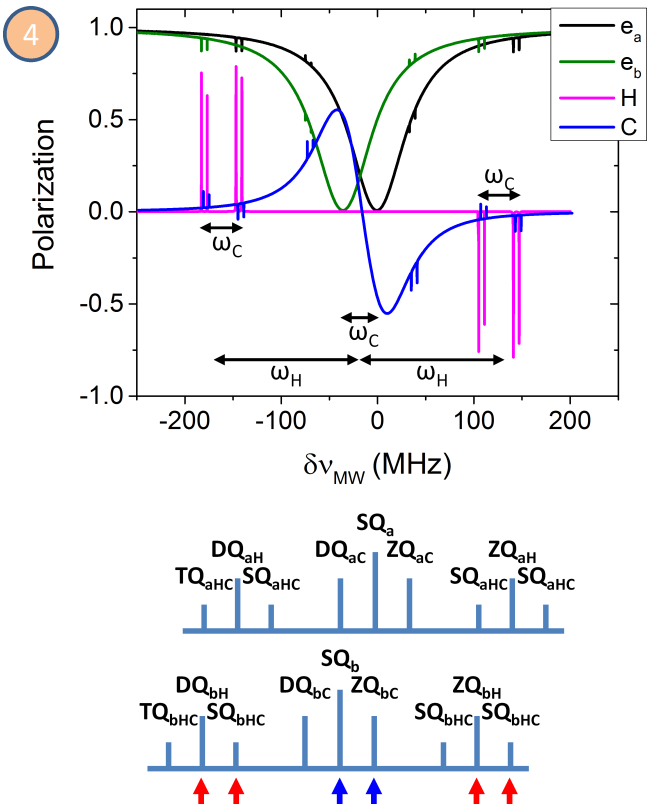

Figure 4: Simulated DNP spectra of the four spin system $\{e_a - e_b - (^1\mathrm{H}, ^{13}\mathrm{C})\}$ at the ^{13}C-CE condition (condition 4). Plotted in the y-axis are the ^{1}H (magenta), ^{13}C (blue) and electron (black, green) polarizations with respect to the electron polarizations at thermal equilibrium. The MW frequency scale is given with respect to $\nu_{ref} = 95 \cdot 10^3$ MHz: $\delta\nu_{MW} = \omega_{MW}/2\pi - \nu_{ref}$. At the bottom are plotted the transitions of the system. The blue arrows mark the overlapping ^{13}C-CE transitions. The red arrows mark the "proton shifted ^{13}C-CE" transitions: DQ_{aH}, DQ_{bH}, ZQ_{aH} and ZQ_{bH}. The parameters used to simulate the DNP spectra are: $T = 10$ K, $\omega_a = 95$ GHz, $\omega_b = 94.9641$ GHz, $\omega_H = 144$ MHz, $\omega_C = 36$ MHz, $D_{ab} = 3$ MHz, $A_{z,aH} = A_{z,bH} = 0$ MHz, $A_{z,aC} = A_{z,bC} = 0$ MHz, $A^{\pm}_{aH} = 0.5$ MHz, $A^{\pm}_{bH} = 0.125$ MHz, $A^{\pm}_{aC} = 0.125$ MHz, $A^{\pm}_{bC} = 0.0625$ MHz, $d_{HC} = 0$ MHz, $\omega_1 = 0.5$ MHz, $T_{1e} = 100$ msec, $T_{1H} = 100$ sec, $T_{1C} = 500$ sec, $T_{1eH} = 1$ sec, $T_{1eC} = 5$ sec, $T_{2e} = 20$ usec, $T_{2n} = 100$ usec. The ^{13}C spectrum was shifted by 2 MHz in the x direction so it would not cover the ^{1}H polarization at the SE transitions.

The indirect ^{13}C−CE :

In order to describe the *i*CE-DNP mechanism in this system, we must extend the four-spin system by adding an electron e_c that interacts with the two existing electrons *via* a weak dipolar coupling that leads to an electron spectral diffusion (eSD) process: $\{e_c \overset{eSD}{\rightarrow} e_a - e_b - (^1\mathrm{H}, ^{13}\mathrm{C})\}$. When the system is at one of the ^{13}C-CE conditions (4,4'), on-resonance MW irradiation at the e_c frequency $\omega_c \neq \omega_a, \omega_b$ can cause a partial depolarization of the other electrons, resulting in $P_a \neq P_b$, when the $[e_c - e_a]$ and $[e_c - e_b]$ eSD polarization exchange rates differ. The electron polarization difference will then result in an enhancement of the ^{13}C nucleus, according to Eq. 1 [17].

The proton shifted direct ^{13}C-CE:

At the two ^{13}C-CE conditions (4,4') we also recognize that the DQ_{eH} and ZQ_{eH} transitions of one electron $e = a, b$ overlap with the $SQ_{e'HC}$ or $TQ_{e'HC}$ transitions of the other electron $e' = b, a$. Thus, at each of the ^{13}C-CE conditions $|\omega_a - \omega_b| = \omega_C$ there are four frequencies where these spectral alignments occur, namely at $\omega_a \pm \omega_H$ and at $\omega_b \pm \omega_H$ (see red arrows in Fig. 4 for (4)). Irradiation at each of these frequencies results in ^{13}C enhancement, as is illustrated in Fig. 4 for (4) with $\omega_a > \omega_b$, with a {positive-negative and positive-negative} pattern for increasing frequency. Note that in this description we ignore splitting caused by the electron dipolar interaction. The distance between the positive and negative polarizations is $\omega_a - \omega_b = \omega_C$ and not $2\omega_C$ as in the three-spin system described above. The effective MW strength at these four transitions is of the order of $\frac{A^{\pm}_{eH}}{\omega_H}\omega_1$, much stronger than $\frac{A^{\pm}_{eH}A^{\pm}_{eC}}{\omega_H\omega_C}\omega_1$in the double-SE case. Thus, while the electrons are at a ^{13}C-CE condition, the MW irradiation on the two ZQ_{eH} or two DQ_{eH} transitions generates ^{1}H and ^{13}C enhancements simultaneously. The proton enhancements are a result of the standard ^{1}H−SE mechanisms and the carbon enhancements are a result of combined {^{1}H-SE+^{13}C-CE} mechanisms. This will be referred to as the "proton shifted ^{13}C-CE" mechanism from here on. A similar derivation can be presented for the other CE condition (4').

The appearance of proton shifted ^{13}C-CE enhancements is a result of a direct saturation of the ZQ_{eH} and DQ_{eH} transitions, together with effective cross-relaxation processes that become active because of state mixing. For example, at the ^{13}C-CE condition, when SQ_a and ZQ_{bC} overlap, the states $|\beta_a\alpha_b\alpha_H\beta_C >$ and $|\alpha_a\beta_b\alpha_H\alpha_C >$ are degenerate and a strong cross-relaxation process, originating from T_{1e} after diagonalization, becomes active at the transition

$$< \beta_a\beta_b\beta_H\alpha_C| \Longleftrightarrow \frac{1}{\sqrt{2}}\{|\beta_a\alpha_b\alpha_H\beta_C > +|\alpha_a\beta_b\alpha_H\alpha_C >\}, \tag{5}$$

which precisely corresponds to the irradiated DQ_{aH} and SQ_{bHC} transitions. The efficiency of this mechanism is best investigated numerically. In the SI a short discussion about the proton shifted ^{13}C-CE is presented together with some numerical simulations.

The proton shifted indirect ^{13}C-CE :

It is also possible to describe the "proton shifted *indirect* ^{13}C-CE mechanism" that results in enhancements, when the MW is applied at $\omega_{MW} \neq \omega_e + \omega_H \pm \omega_C$ or $\omega_{MW} \neq \omega_e - \omega_H \pm \omega_C$, on a system at its ^{13}C-CE condition, $|\omega_a - \omega_b| = \omega_C$. In order to do so we again must extend the spin system, this time by adding a third electron, e_c, that is hyperfine coupled to a ^{1}H nucleus and does not have a significant dipolar interaction with e_a and e_b: $\{^1\mathrm{H} - e_c \overset{eSD}{\rightarrow} e_a - e_b - (^1\mathrm{H}, ^{13}\mathrm{C})\}$. MW irradiation at ω_{MW}=$\omega_C \pm \omega_H$ (ZQ_{cH} or DQ_{cH}) will partially saturate e_c, which in turn will depolarize e_a and e_b differently ($P_a \neq P_b$) when the $[e_c - e_a]$ and $[e_c - e_b]$ eSD polarization exchange rates differ. The ^{13}C polarization will then get a value according to Eq. 1 [17, 60]. This a direct analog to the ^{13}C-*i*CE described above, but for the "proton shifted" case.

In powder samples containing ^{1}H and ^{13}C nuclei with inhomogeneously broadened EPR spectra that are broader than ω_C and narrower than ω_H, excitation of the DQ_{eH} or ZQ_{eH}

transitions outside the EPR spectrum causes electron depolarization via the standard ^{1}H-SE process. This depolarization gets extended over the whole EPR spectrum by the eSD process and generates an electron polarization gradient over the whole sample [60]. For electrons at a ^{13}C-CE conditions this gradient can generate ^{13}C polarization and therefore we refer to it as the "proton shifted *indirect* ^{13}C-CE" coming from the $\{^1$H-SE+^{13}C-*i*CE$\}$ mechanism.

3.3 The ^{1}H-CE conditions at {2,2'}

The ^{1}H-CE conditions (2,2'), with $|\omega_a - \omega_b| = \omega_H$, are analogous to the ^{13}C-CE conditions described above. Typical enhancement profiles are drawn in the SI and show the standard ^{1}H-CE enhancement when irradiating on the SQ_e electron transitions and standard SE enhancements at $\pm\omega_H$ away from these transitions. In this system it is also possible to find the "carbon shifted ^{1}H-CE", i.e.^{1}H enhancement when irradiating at the DQ_{eC} and ZQ_{eC} transitions at $\omega_a \pm \omega_C$ and $\omega_b \pm \omega_C$ (red arrows in figure in the SI). This is equivalent to the proton shifted ^{13}C-CE, though with the parameters chosen the effect is not visible. Moreover, both the *indirect* ^{1}H-CE and the "carbon shifted *indirect* ^{1}H-CE" can be described in a direct analog to what was described above.

3.4 The $\{^1\mathrm{H} -^{13}\mathrm{C}\}$ heteronuclear CE mechanism {1,1' ; 3,3'}

3.4.1 Steady state ^{1}H-DNP and ^{13}C-DNP enhancements

In the four-spin system, $\{e_a - e_b - (^1\mathrm{H},^{13}\mathrm{C})\}$, we recognize also two high-order CE conditions: $|\omega_a - \omega_b| = \omega_H - \omega_C$ and $|\omega_a - \omega_b| = \omega_H + \omega_C$, respectively labeled (3,3') and (1,1') in Fig. 3. These conditions are different from the other conditions in the sense that they are dependent on the two Larmor frequencies of the nuclei. We therefore expect them to result in DNP effects that correlate the two nuclear polarizations directly. Although no experimental evidence of these effects will be shown here, we find it important to discuss their main DNP characteristics for completeness of this discussion and will leave experimental verifications to a future publication.

At condition (3) transition SQ_a overlaps with SQ_{bHC}, and SQ_b overlaps with SQ_{aHC} and as a result a degeneracy occurs between the states $|\beta_b\alpha_a\beta_H\alpha_C>$ and $|\alpha_b\beta_a\alpha_H\beta_C>$. In addition the DQ_{aH} and DQ_{bC} transitions overlap, as do the ZQ_{aH} and ZQ_{bC} transitions. These conditions are depicted in Fig. 3. Similar conditions can be derived for the other high order CE conditions (1,1',3') and the results are summarized in Table 1.

	CE-conditions $\omega_a - \omega_b =$	degenerate states	overlapping CE transition	overlapping transitions
1	$\omega_H + \omega_C$	$\|\beta_a\alpha_b\beta_H\beta_C> -$ $\|\alpha_a\beta_b\alpha_H\alpha_C>$	SQ_a and SQ_{bHC}, SQ_b and TQ_{aHC}	DQ_{aH} and ZQ_{bC}, DQ_{aC} and ZQ_{bH}
1'	$-\omega_H - \omega_C$	$\|\beta_a\alpha_b\alpha_H\alpha_C> -$ $\|\alpha_a\beta_b\beta_H\beta_C>$	SQ_a and TQ_{bHC}, SQ_b and SQ_{aHC}	ZQ_{aC} and DQ_{bH}, ZQ_{aH} and DQ_{bC}
3	$\omega_H - \omega_C$	$\|\beta_a\alpha_b\beta_H\alpha_C> -$ $\|\alpha_a\beta_b\alpha_H\beta_C>$	SQ_a and SQ_{bHC}, SQ_b and SQ_{aHC}	DQ_{aH} and DQ_{bC}, ZQ_{aH} and ZQ_{bC}
3'	$-\omega_H + \omega_C$	$\|\beta_a\alpha_b\alpha_H\beta_C> -$ $\|\alpha_a\beta_b\beta_H\alpha_C>$	SQ_a and SQ_{bHC}, SQ_b and SQ_{aHC}	DQ_{aC} and DQ_{bH}, ZQ_{aC} and ZQ_{bH}

Table 1: Summary of the high order CE conditions, including the degenerate states, the overlapping transitions which cause the degeneracy and additional overlapping transitions.

Inspection of the table reveals that these heteronuclear CE conditions degeneracies occur between states that differ in both of the electron states, $|\alpha_a\beta_b> \leftrightarrow |\beta_a\alpha_b>$, and simultaneously in both of the nuclear states, $|\alpha_H\beta_C> \leftrightarrow |\beta_H\alpha_C>$ or $|\alpha_H\alpha_C> \leftrightarrow |\beta_H\beta_C>$. No additional cross-relaxation rates were added to the system, but as a result of the mixing between these states, cross-relaxation processes induced by the spin-lattice relaxations, T_{1a} and T_{1b}, as well as, possibly, by hyperfine fluctuations, creating heteronuclear cross-relaxation mechanisms (involving electron and both types of nuclear spin flips), become significant. These processes complicate the spin dynamics during MW irradiation and numerical spin-model calculations of the nuclear enhancements are necessary to verify the consequences of MW irradiation on a four-spin system at one of its heteronuclear CE conditions. Typical results of frequency swept ^{1}H-DNP and ^{13}C-DNP spectra are shown in Fig. 5 at condition (3) and in the SI at condition (1). The parameters used for the simulation are given in the figure captions. These figures show that at one of the heteronuclear CE conditions, MW irradiation results in ^{1}H-DNP and ^{13}C-DNP spectra that exhibit broad CE type enhancements at the SQ frequencies (blue arrows) and narrow SE features at the frequencies of all ZQ_{en} and DQ_{en} transitions.

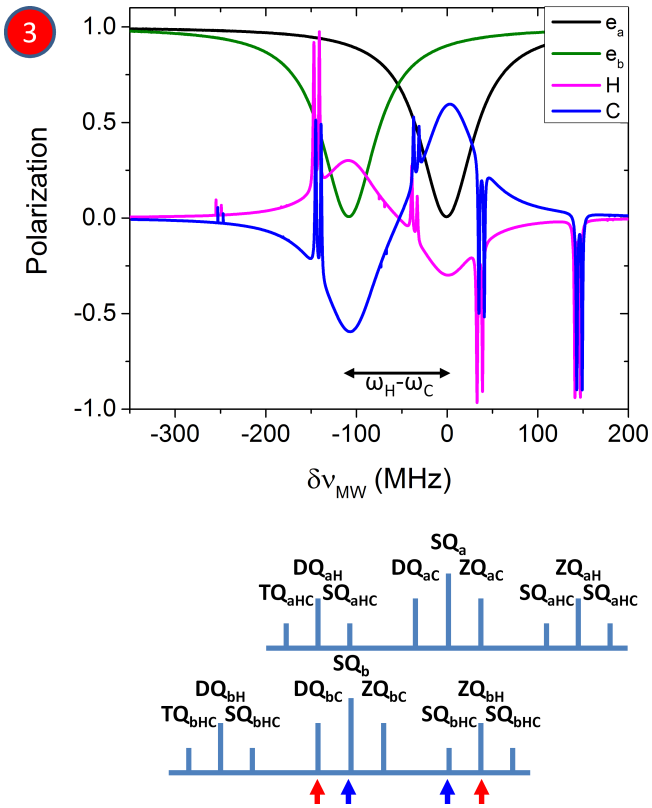

Figure 5: Simulated DNP spectra of the four spin system $\{e_a - e_b - (^1\mathrm{H}, ^{13}\mathrm{C})\}$ at the ^{1}H-^{13}C-CE condition (condition 3). Plotted in the y-axis are the ^{1}H (magenta), ^{13}C (blue) and electron (black, green) polarizations with respect to the electron polarizations at thermal equilibrium. The MW frequency scale is given with respect to $\nu_{ref} = 95 \cdot 10^3$ MHz: $\delta\nu_{MW} = \omega_{MW}/2\pi - \nu_{ref}$. At the bottom are plotted the transitions of the system. The blue arrows mark the overlapping high order CE transitions. The red arrows mark the overlapping transitions: DQ_{aH} with DQ_{bC} and ZQ_{aH} with ZQ_{bC}. The parameters used to simulate the DNP spectra are: $T = 10$ K, $\omega_a = 95$ GHz, $\omega_b = 94.8920$ GHz, $\omega_H = 144$ MHz, $\omega_C = 36$ MHz, $D_{ab} = 3$ MHz, $A_{z,aH} = A_{z,bH} = 0$ MHz, $A_{z,aC} = A_{z,bC} = 0$ MHz, $A^{\pm}_{aH} = 0.5$ MHz, $A^{\pm}_{bH} = 0$ MHz, $A^{\pm}_{aC} = 0.125$ MHz, $A^{\pm}_{bC} = 0$ MHz, $d_{HC} = 0$ MHz, $\omega_1 = 0.5$ MHz, $T_{1e} = 100$ msec, $T_{1H} = 100$ sec, $T_{1C} = 200$ sec, $T_{2e} = 20$ usec, $T_{2n} = 100$ usec. The ^{13}C spectrum was shifted by 2 MHz in the x direction so it would not cover the ^{1}H polarization at the SE transitions.

In a direct analogy to Eq. 1, it is also possible to write a similar equation describing the nuclear polarizations as a function of the electron polarizations at the heteronuclear CE conditions. When the system is at one of the heteronuclear CE conditions both nuclei get polarized with steady state values that can be simulation, and that satisfy the relation:

$$P_{^1H} \pm P_{^{13}C} = \frac{P_a - P_b}{1 - P_a P_b} \tag{6}$$

for $|\omega_a - \omega_b| = |\omega_H \pm \omega_C|$, respectively. These simulations also showed that the individual values of $P_{^1H}$ and $P_{^{13}C}$ are dependent on the spin lattice relaxation parameters, T_{1H} and T_{1C}, and satisfy the following dependencies:

$$P_{^1\mathrm{H}} = \frac{P_a - P_b}{(1 - P_a P_b)(1 + \frac{T_{1C}}{T_{1H}})} \tag{7}$$

$$P_{^{13}\mathrm{C}} = \pm \frac{P_a - P_b}{(1 - P_a P_b)(1 + \frac{T_{1H}}{T_{1C}})} \tag{8}$$

for $|\omega_a - \omega_b| = |\omega_H \pm \omega_C|$, respectively. Thus for $T_{1C} \gg T_{1H}$ most of the polarization resides at the ^{13}C nucleus, and the heteronuclear CE does hardly affects the ^{1}H nucleus. These equalities (Eqs. 1, 7 and 8) have been verified by a large set of simulations for systems with different parameters. They are correct as long as the MW irradiation equally affects the two SQ_e transitions of each electron equally (splitted due to the electron-electron dipolar interaction and the secular term of the hyperfine interaction) [17]. Moreover, Eq. 1 is correct also at thermal equilibrium while Eqs. 7 and 8 are correct only during on-resonance MW irradiation on either electron e_a or electron e_b). Examples of these observations are shown in SI.

3.4.2 The time evolution of the ^{1}H-DNP and ^{13}C-DNP enhancements

The buildup of the polarization over time during MW irradiation and the polarization decay after switching it off can also be studied in the four-spin system at one of its heteronuclear CE conditions. To that aim, we simulated, as an example, the time behavior of the nuclear polarizations during and after MW irradiation on the SQ_b frequency of a system slightly removed from the heteronuclear CE condition. The results in Figs 6a,c are from a system close to condition (3) and Figs. 6b,d close to condition (1).

As can be seen in Fig. 6a,b, due to the strong state mixing both ^{1}H and ^{13}C polarizations buildup in a time of the order of T_{1e}. The polarizations then redistribute in the timescale of the order of T_{1H} ($< T_{1C}$) to reach their DNP steady state values. After shutting off the MW irradiation the nuclei reach equal or opposite average polarization in a time much longer than T_{1e}, which is followed by the decay of both nuclear polarization to their thermal equilibrium values in the timescale of the order of T_{1H} ($< T_{1C}$). The fact that the system is not exactly at a heteronuclear CE condition results in a slight slowing down of the equilibration processes between the nuclei.

At the heteronuclear CE conditions polarization exchange processes between the nuclei can take place. This can be demonstrated by saturating the ^{13}C polarization immediately after the MW irradiation is switched off and by following the temporal ^{1}H and ^{13}C polarizations in the absence of MW irradiation. A simulation of such an experiment is shown in Figs. 6c,d. After saturation of the ^{13}C nucleus, the nuclei again reach an equal or opposite polarization in a short time. Thus we detect a partial recovery of the ^{13}C polarization on account of the ^{1}H polarization. It is worth noting that when the ^{1}H is selectively saturated its polarization also recovers to some extent, on account of the ^{13}C polarization, however when both nuclei are polarized and then fully saturated none of the polarizations recover beyond their thermal values.

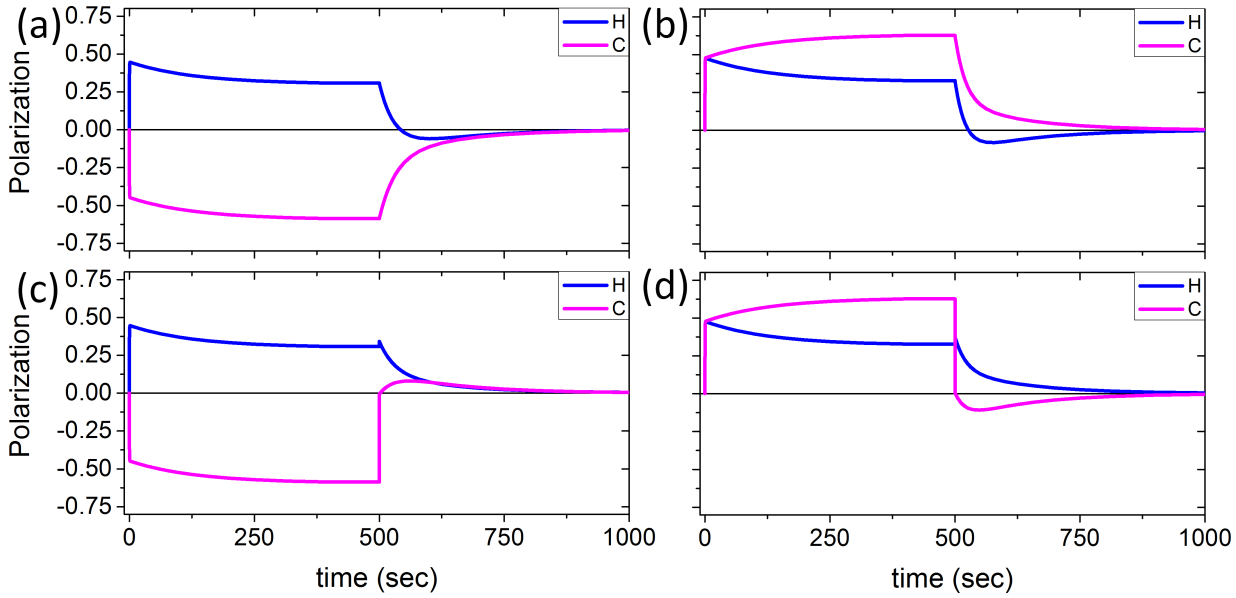

Figure 6: Simulated DNP buildup and decay curves are plotted for the four spin system $\{e_a - e_b - (^1\mathrm{H}, ^{13}\mathrm{C})\}$, in (a) and (c) at the ^{1}H-^{13}C-CE condition (3) and in (b) and (d) at the ^{1}H-^{13}C-CE condition (3). In all four panels polarization buildup curves are plotted up to t_{MW} =500 sec, after which in (a,b) we plot polarization decay curves and in (c,d) we plot decay curves after saturation of the ^{13}C nucleus. Plotted are the ^{1}H (magenta) and ^{13}C (blue) polarizations with respect to the electron polarizations at thermal equilibrium. The parameters used to simulate the DNP spectra are: For condition (3): $\omega_{MW} = \omega_b$ MHz, $\omega_a = 95$ GHz, $\omega_b = 94.8920$ GHz. For condition (1): $\omega_{MW} = \omega_b$ MHz, $\omega_a = 95$ GHz, $\omega_b = 94.820$ GHz. For both conditions: $T = 10$ K, $\omega_H = 144$ MHz, $\omega_C = 36$ MHz, $D_{ab} = 3$ MHz,$A_{z,aH} = A_{z,bH} = 0$ MHz, $A_{z,aC} = A_{z,bC} = 0$ MHz, $A^{\pm}_{aH} = 0.5$ MHz, $A^{\pm}_{bH} = 0$ MHz, $A^{\pm}_{aC} = 0.125$ MHz, $A^{\pm}_{bC} = 0$ MHz, $d_{HC} = 0$ MHz, $\omega_1 = 0.5$ MHz, $T_{1e} = 100$ msec, $T_{1H} = 100$ sec, $T_{1C} = 200$ sec, $T_{2e} = 20$ usec, $T_{2n} = 100$ usec.

3.4.3 The two spin indirect $\{^1\mathrm{H} - ^{13}\mathrm{C}\}$-CE mechanism (1,1' ; 3,3')

In order to incorporate the enhancements obtained when the spin system is at one of its heteronuclear CE conditions (1,1'; 3,3') into the *indirect*-CE mechanisms, we extend the four spin system by adding an additional electron that is very weakly coupled to the two existing electrons and leads to spectral diffusion, $\{e_c \overset{eSD}{\rightarrow} e_a - e_b - (^1\mathrm{H}, ^{13}\mathrm{C})\}$. Irradiating at the resonance frequency $\omega_{MW} = \omega_c$ of e_c can again create a partial depolarization of e_a and e_b with $P_a \neq P_b$. When the system is at one of the heteronuclear CE conditions both nuclei get polarized with steady state values given according to Eqs. 6, 7 and 8.

Up to this point we concentrated on defining the effects seen in small spin systems. In a real sample with many electrons at different frequencies we expect that both of these heteronuclear CE (1,1',3,3') are active simultaneously. As a result we should observe polarization exchange phenomena between the two types of nuclei in samples that are both polarized. Many observations are reported in the literature that have shown connectivity between nuclear polarizations and that were interpreted using TM mechanisms [37, 38]. The *i*CE extension of the heteronuclear CE mechanism must thus be further developed in an effort to verify which of the observed

polarization cross-talk phenomena can be explained by it. The present discussion must, however, be continued on the basis of experimental observations because of the complexity of the spin dynamics of systems at these heteronuclear CE conditions.

4 Experimental results

In the following section we will describe experimental EPR, NMR and DNP results from a sample of 15 mM trityl. In this work we will express the frequencies in units of MHz, with respect to a reference frequency $\nu_{ref} = 94.863$ GHz such that instead of ω_ξ we will write $\delta\nu_\xi = \omega_\xi/2\pi - \nu_{ref}$. In addition, in the next part of the work the experimental MW irradiation frequency will be referred to as ω_{excite}, such that it's frequency will be denoted as $\delta\nu_{excite} = \omega_{excite}/2\pi - \nu_{ref}$.

4.1 DNP spectra

^{13}C-DNP spectra of the trityl sample were measured at 6.5 K with a MW irradiation time of t_{MW}=320 sec and at 30 K with $t_{MW} = 900$ sec, and are shown in Fig. 7a. In the center of the spectrum we observe a regular ^{13}C-DNP lineshape with positive enhancement at the lower frequency and negative enhancement at the high frequency range. Additionally, we observe spectral features at the sides of the main DNP spectrum, outside of the EPR spectrum. These features can be divided into two sets: one appearing around ±144 MHz, with typical positive-negative DNP spectral lineshapes, and another around +100 MHz and −91 MHz, also showing positive-negative lineshapes. Note that the outer pair of lineshapes are centered at the proton Larmor frequency $\omega_H = 144$ MHz, while the inner pair of shapes appear at frequencies which do not correspond to any Larmor frequency in the system. Both the inner and the outer pairs have positive and negative enhancements separated by $\omega_C/2\pi = 36$ MHz. Although they were measured far from the steady state of the system ($t_{MW} < T_{1C}$), the buildup time experiments suggest that their shapes resemble the shape of the steady state DNP spectra. As can be seen in Fig. 7a, there is no change in the relative intensity of the outer pair of features in the ^{13}C-DNP spectrum between 6.5 K and 30 K. Because the thermal equilibrium signal was not measured due to signal to noise ratio problems, the DNP spectra in Fig. 7a are normalized and do not show the actual enhancement values.

In order to identify the nature of the inner lineshapes, the sample was sonicated as described in Section 2.1. ^{13}C-DNP spectra measured at 10 K before and after sonication are shown in the SI. After sonication the inner pair of spectral features disappeared, but the outer pair remained. From this we must conclude that the inner and outer spectral features are separate effects. The disappearance of the inner pair after sonication suggests that the inner set is related to a dimerization or clustering of the trityl radicals during sample preparation, causing large electron-electron interactions similar to what was described in Ref. [67]. After sonication these dimers or clusters are largely disrupted to a level that the inner DNP effects disappear. The presence (or absence) of these dimers or clusters did not influence the EPR spectra, which

suggests their low abundance (EPR data not shown). All other experimental data in this work were conducted on a non-sonicated sample.

The non-sonicated steady state ^{1}H-DNP spectra at 6.5 K and 30 K are shown in Fig. 7b. Here we clearly see that the ^{1}H-DNP mechanism is determined by the SE, showing strong hyperpolarizations outside the EPR spectrum position. The width of the positive and negative enhancement profiles increases slightly as the temperature is lowered, likely a consequence of the lengthening of the nuclear relaxation times. There is also a small feature observed at the center of the ^{1}H-DNP spectrum though the effect is too small to be considered further in this work and must be studied with care.

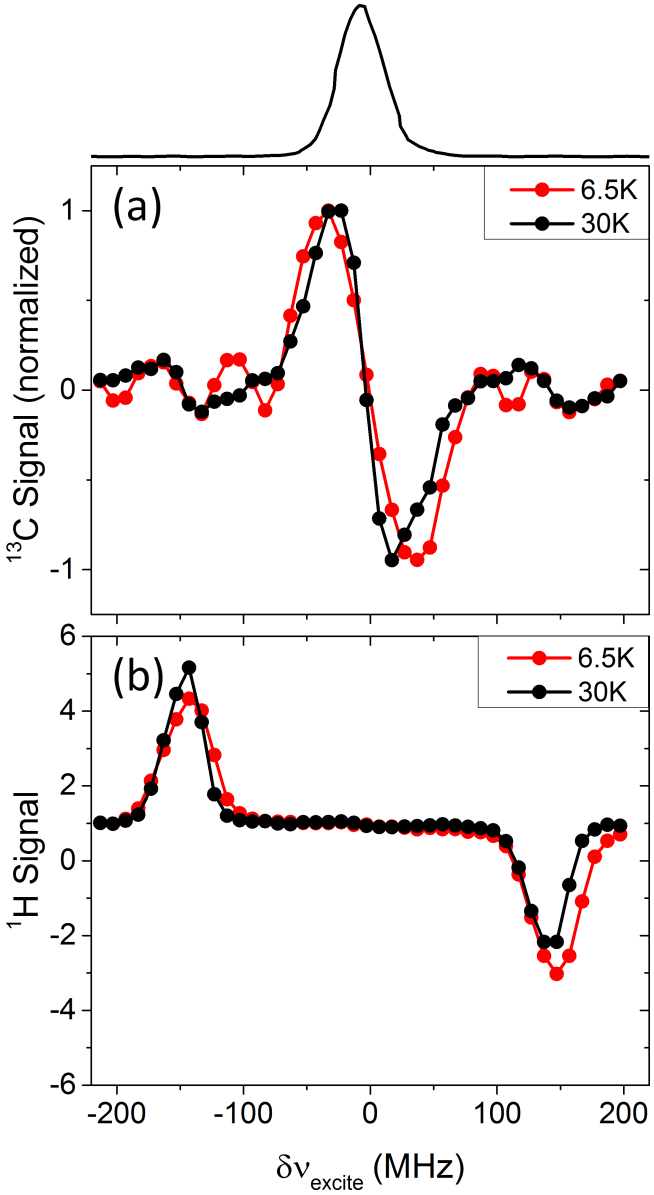

Figure 7: (a) Normalized (a) ^{13}C-DNP spectra and (b) ^{1}H-DNP spectra measured at 6.5 K (red) and 30 K (black). The ^{13}C-DNP spectra at 6.5 K were measured with t_{MW} =320 sec and the spectrum at 30 K was measured with t_{MW} = 900 sec. The ^{1}H-DNP spectra were all measured with t_{MW} =40 sec at 6.5 K and t_{MW} =60 sec at 30 K. Plotted above is the ED-EPR spectrum. The parameters of the experiments are listed in the Methods section. The lines in this figure are to guide the eye. The MW frequency scale is given with respect to $\nu_{ref} = 94.863 \cdot 10^3$ MHz.

4.2 Relaxation times

The electron, proton and carbon spin-lattice relaxation times T_{1e}, T_{1H}, T_{1C}, and the ^{13}C-DNP buildup times at $\delta\nu_{excite} = -33$ MHz and $\delta\nu_{excite} = -163$ MHz, $T_{bu,33}$ and $T_{bu,163}$, respectively, were also recorded. All three T_1 relaxation times increase as the temperature is lowered (see Table 2). The buildup times at the two frequencies are equal, within experimental error, at all temperatures and at 6.5 K they are shorter than T_{1C} while at at 30 K they become of the order of T_{1C}. Because $T_{bu,33} \approx T_{bu,163}$ at all temperatures, significant changes in the DNP lineshapes are not expected during their buildup and the recorded normalized spectra should resemble the normalized steady state enhancement lineshapes.

T	T_{1e} (msec)	T_{1H} (sec)	T_{1C} (sec)	$T_{bu,33}$(sec)	$T_{bu,163}$(sec)
6.5 K	512±22	215±43	2048±213	1473±67	1627±178
30 K	46±2	34±4	1087±270	826±140	495±300

Table 2: Relaxation times, DNP buildup times as a function of temperature. The errors represent the 95% confidence interval of the timescale parameters resulting from the fitting procedure of the electron and nuclear saturation recovery curves, DNP buildup curves and DNP decay curves.

4.3 ELDOR spectra

In addition to the DNP spectra, we measured ELDOR spectra as a function of different detection frequencies $\delta\nu_{detect}$.

Each ELDOR spectrum, $E^{exp}_{excite}(\delta\nu_{excite})$, shows the EPR echo intensity detected, at a frequency $\delta\nu_{detect}$, as a function of the frequency $\delta\nu_{excite}$ of a MW pulse applied prior to the echo detection. These spectra can be seen in Fig. 8. In this figure the ELDOR spectra are normalized with respect to thermal equilibrium electron polarization at $\delta\nu_{detect}$. As can be clearly seen, when $\delta\nu_{excite} = \delta\nu_{detect}$ the echo intensity becomes zero, indicating that the electrons at that frequency become saturated due to on-resonance irradiation on the SQ transition of the electrons at $\delta\nu_{detect}$. When $\delta\nu_{exite}$ is far from $\delta\nu_{detect}$ the detected electrons stay fully polarized. When the excitation frequency is $\delta\nu_{detect} \pm \delta\nu_H$ a partial saturation of the SQ electron transitions at $\delta\nu_{detect}$ is detected due to irradiation on the DQ$_{eH}$ and ZQ$_{eH}$ transitions. Irradiation at the DQ$_{eC}$ and ZQ$_{eC}$ frequencies of the ^{13}C nuclei, $\delta\nu_{detect} \pm \delta\nu_C$, did not result in visible effects on the echo signals. Note that at 30 K there are interesting effects of hyperpolarization and depolarization of the electron, previously observed by Hovav et al. in ELDOR a sample of trityl with natural abundance ^{13}C [60].

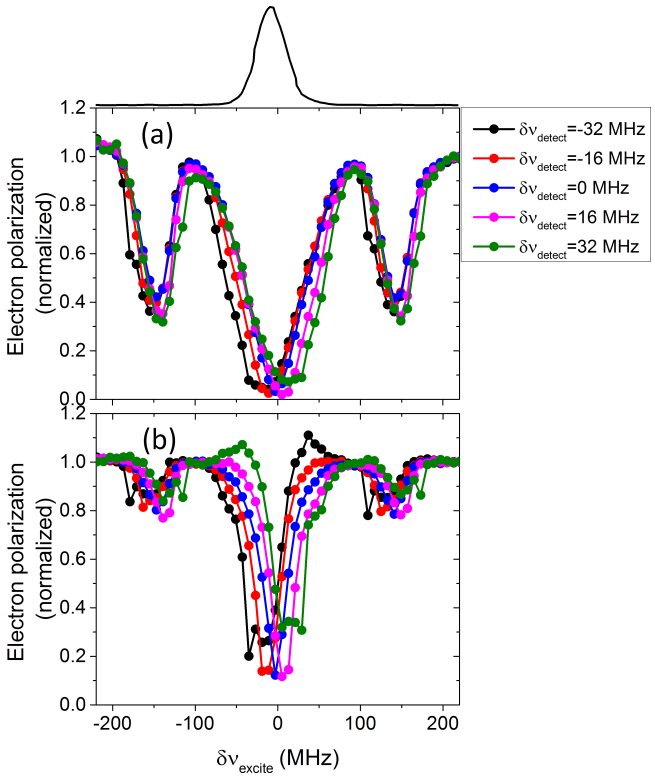

Figure 8: Experimental ELDOR spectra at (a) 6.5 K and (b) 30 K. The spectra were measured at several detection frequencies: (black) $\delta\nu_{detect}$ =-32 MHz, (red) $\delta\nu_{detect}$ =-16 MHz, (blue) $\delta\nu_{detect}$ =0 MHz, (magenta) $\delta\nu_{detect}$ =16 MHz and (green) $\delta\nu_{detect}$ =32 MHz. Plotted above is the ED-EPR spectrum of the sample. The MW frequency scale is given with respect to $\nu_{ref} = 94.863 \cdot 10^3$ MHz.

The set of ELDOR spectra, $E^{exp}_{excite}(\delta\nu_{excite})$, measured at different $\delta\nu_{detect}$ frequencies can be combined to generate a 2D ELDOR contour plot of the normalized electron polarization as a function of the detection frequency $\delta\nu_{detect}$ and the excitation frequencies $\delta\nu_{excite}$: $E_e(\delta\nu_{excite}, \delta\nu_{detect})$. Simulations of $P_e(\delta\nu_{detect}; \delta\nu_{excite})$ contours will give the electron polarization across the EPR frequency $\delta\nu_{detect}$ for different $\delta\nu_{excite}$ frequencies [60]. These electron polarization profiles will then be used to calculate the effect of the electron depolarization on the shapes of the DNP spectra [17], as will be discussed in the next section.

5 Analysis of the DNP Spectra

At this point we consider which of the mechanisms discussed in Section 3 are responsible for the features observed in the DNP spectra. It is already possible to narrow down the list just by realizing that the trityl EPR linewidth is at its base ∼100 MHz, which is smaller than the ^{1}H Larmor frequency, ω_H =144 MHz, which means that the ^{1}H-DNP spectrum in Fig. 7b must be solely determined by the SE mechanism. The ^{13}C Larmor frequency is ω_C =36 MHz, which means that the only CE conditions possible in the sample are the regular ^{13}C-CE conditions with $|\omega_a - \omega_b| = \omega_C$ (4 and 4' in Fig. 3). Because the heteronuclear CE conditions cannot be satisfied ($|\omega_H - \omega_C|$ = 108 MHz and $|\omega_H + \omega_C|$ = 180 MHz), the only possible active DNP mechanisms in the ^{13}C-DNP spectrum in Fig. 7a are the SE, the standard *d*CE and *i*CE, the

double-SE and the proton shifted dCE and iCE. The proton shifted ^{13}C-iCE can be considered as part of the general ^{13}C-iCE since the ^{1}H-SE contributions to the electron depolarization are included in the overall electron polarization distribution.

In our previous studies we neglected the influence of the eSD process on the electron polarizations when calculating the basic lineshapes of the different DNP mechanisms [49, 50, 54, 55]. However, in the present study we take this into account and we calculate the basic ^{1}H-SE-DNP, ^{13}C-SE-DNP, ^{13}C-CE-DNP and ^{13}C-iCE-DNP lineshapes, using electron polarization profiles derived from ELDOR experiments and the equations presented in Section 4.3.

5.1 Simulating electron polarization distributions

The polarization of the electrons $P_e(\delta\nu_{detect};\delta\nu_{excite})$ at different frequencies $\delta\nu_{detect}$ during MW irradiation at $\delta\nu_{excite}$ can be derived from the 2D ELDOR experiments resulting in the polarizations $E^{exp}_{excite}(\delta\nu_{excite})$ as a function of $\delta\nu_{excite}$ for different detection frequencies $\delta\nu_{detect}$, as described in Section 2.3. These polarization profiles can be calculated by solving a set of coupled rate equations for the polarizations $P_{e,j}$ of the electrons in fixed frequency bins j, and an average nuclear polarization P_n representing all nuclei of one type in the system. Each bin j has a frequency $\delta\nu_j$, a width Δ_{bin} and a relative intensity f_j, composing the normalized EPR spectrum, as was recently described in [60]. The rate equation model includes the effects of the MW irradiation, the eSD process and the relaxation times of the electrons and nuclei, and in addition takes into account the EPR lineshape of the electrons and their relative concentration with respect to the nuclear concentration. Thus the parameters entering this model are MW intensity ν_1, a coefficient Λ^{eSD} defining the eSD process and determining the maximum polarization exchange rate between neighboring bins, T^{eSD}_{max}, the relaxation times T_{1e}, T_{2e} and T_{1n} and the normalized EPR lineshape $f(\nu_e)$. In addition the SE is taken into account by adding effective MW irradiation rates to the coupled equations, determined by a pseudo-hyperfine coefficient $\overline{A}$ that represents the interaction between the electrons and the nuclei. To apply this model in order to analyze the ELDOR data in our case, the nuclear parameters used were those of the proton.

Solving these rate equations results in the electron polarization $P_{e,j}(t)$ of each bin for a fixed MW frequency $\delta\nu_{excite}$. By using the measured rate constants (T_{1e} and T_{1n}) and fitting the parameters (T_{2e}, Λ^{eSD} and $\overline{A}$) it is then possible to simulate ELDOR spectra $E^{sim}_{excite}(\delta\nu_{excite})$ that fit the experimental data, $E^{exp}_{excite}(\delta\nu_{excite})$ for the different $\delta\nu_{detect}$ values. With the same parameters we can generate the electron polarization profiles, $P_e(\delta\nu_{detect};\delta\nu_{excite})$. These profiles form the basis from which the basic DNP lineshapes of the different mechanisms can be derived.

Using this procedure, and considering only the abundant ^{1}H nuclei in the sample, the temperature dependent ELDOR spectra of trityl (see Fig. 8) were analyzed and the results for 6.5 K are shown in of Fig. 9. The fitting of the 30K data is shown in the SI. Overall, the fits are good in all cases, though they are better the closer $\delta\nu_{detect}$ is to the center of the EPR spectrum. At 30 K the fitting does not look as good as at the lower temperature because of additional effects of electron hyperpolarization and depolarization effects that were previously described

in Ref. [60]. The ^{1}H-SE mechanism manifests itself in strong depolarizations at the frequencies of the DQ_{eH} and ZQ_{eH} transitions. The ^{13}C-SE transitions are not visible and therefore an addition of a ^{13}C polarization to the rate equations was not necessary. The parameters used for these fits are given in Table 3. The large increase in T_{1e} when going from 30 K to 6.5 K must be the cause of the large change in the widths of the ELDOR spectra. This change necessitated a change in the fitting parameter Λ^{eSD}as a function of temperature, with a larger value in the 30 K case, in order to make up for the shortening of T_{1e}. The $\overline{A}$ parameter were chosen to be independent of temperature. At 6.5 K, Λ^{eSD} can be varied from about 0.3 to 0.75 μsec^{-3}, and T_{2e}, can be varied from 85 to 195 μsec without significantly affecting the ELDOR fits. At 30 K the ranges are 2 to 4.5 μsec^{-3} for Λ^{eSD} and 65 to 150 μsec for T_{2e}. The two sets of simulated ELDOR spectra can be combined to give simulated 2D ELDOR contours (shown in the SI) that will be used for the simulations of the ^{1}H and ^{13}C DNP spectra at the two temperatures.

T (K)	T_{1e} (msec)	T_{1n} (sec)	T_{2e} (μsec)	$\overline{A}$ (MHz)	Λ^{eSD} (μsec^{-3})	T^{eSD} (msec)	^{13}C-SE	^{13}C-iCE
6.5	534	215	130	0.1	0.5	0.1686	0.45	0.65
30	46	34	100	0.1	3	0.0281	0.45	0.75

Table 3: The parameters used to calculate the ELDOR spectra and the contribution of SE and iCE (at the maximum of each, respectively) needed in order to fit the DNP spectra. At both temperatures the MW irradiation strength was 0.6 MHz and $\Delta_{bin} = 2$ MHz.

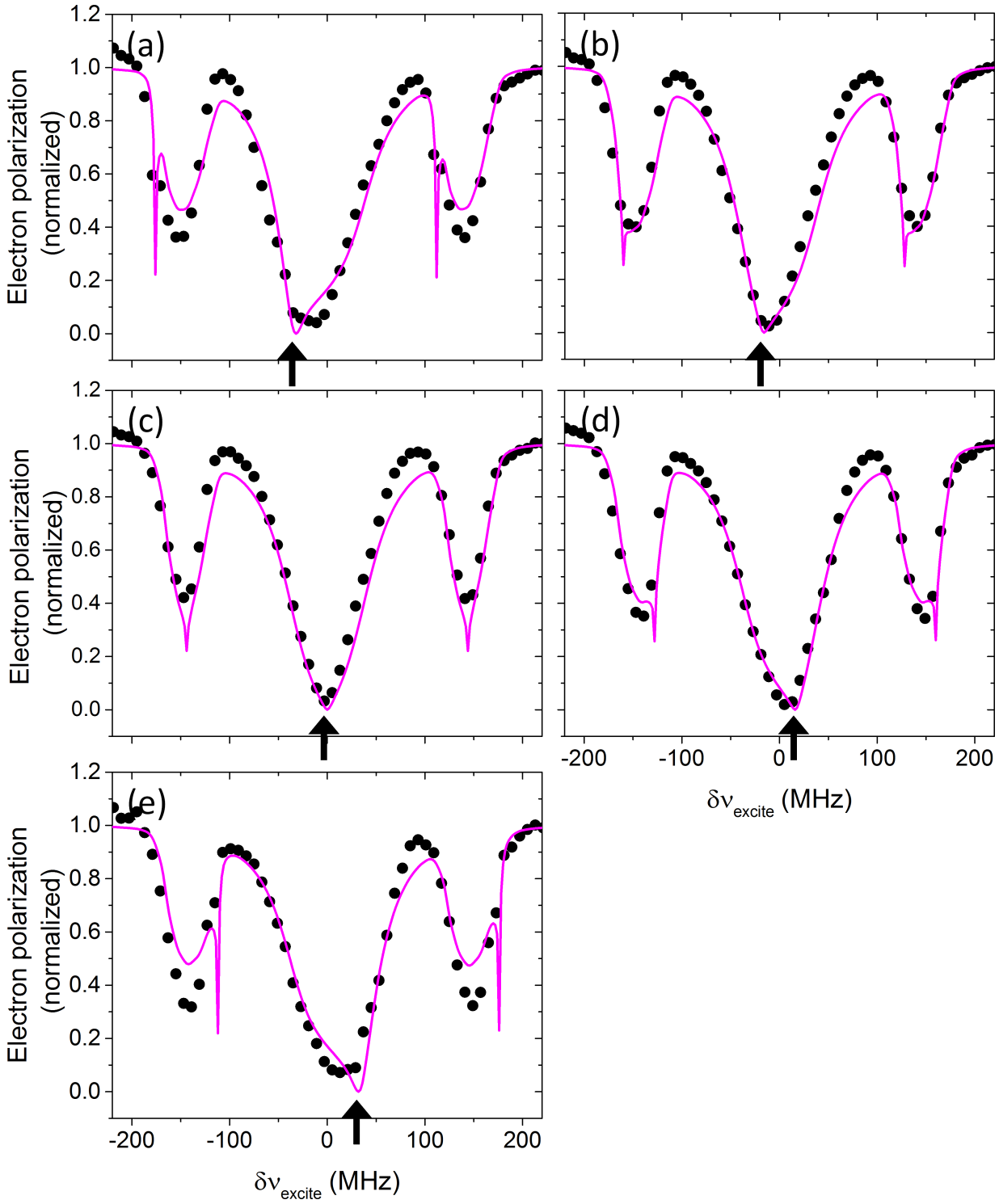

Figure 9: Fitting of the ELDOR spectra measured at 6.5 K and at different ω_{detect} frequencies, marked by the black arrows. The experimental data (black circles) are overlaid on the fits (magenta lines). The black arrows mark the detection frequencies: (a) -32 MHz, (b) -16 MHz, (c) 0 MHz, (d) 16 MHz and (e) 32 MHz. The parameters used for the fitting are given in Table 3. The MW frequency scale is given with respect to $\nu_{ref} = 94.863 \cdot 10^3$ MHz.

5.2 Simulation of the basic SE-DNP, CE-DNP and iCE-DNP spectra

After calculating the $P_e(\delta\nu_{detect};\delta\nu_{excite})$ profiles, we can use them to simulate the basic DNP lineshapes of the SE, CE, and iCE.

The MW frequency dependence of the ^{1}H and ^{13}C SE-DNP lineshapes can be obtained by using these profiles and assuming that the nuclear polarization is proportional to the polarizations of the electrons contributing to the SE enhancement and their relative numbers [17]:

$$S^n_{SE}(\delta\nu_{excite}) = N^{-1}_{SE}\{f_{e-}P_e(\delta\nu_{excite} - \delta\nu_n;\delta\nu_{excite}) - f_{e+}P_e(\delta\nu_{excite} + \delta\nu_n;\delta\nu_{excite})\} \quad (9)$$

where for $n =^1$ H or ^{13}C, and the relative intensities $f_{e\pm}$ are probabilities to find electrons at $\delta\nu_{excite} \pm \omega_n$, respectively, calculated from the normalized ED-EPR spectrum (shown in Figs. 7 and 8). N^{-1}_{SE} is a normalization factor for each $S^n_{SE}(\delta\nu_e)$.

The ^{1}H-DNP and ^{13}C-dCE-DNP lineshapes can be calculated as following:

$$S^n_{dCE}(\delta\nu_{excite}) = N^{-1}_{dCE}f_e\{f_{e-}s_{CE-}(\delta\nu_{excite}) - f_{e+}s_{CE+}(\delta\nu_{excite})\} \quad (10)$$

with

$$s_{CE\pm}(\delta\nu_{excite}) = \frac{P_e(\delta\nu_{excite};\delta\nu_{excite}) - P_e(\delta\nu_{excite} \pm \delta\nu_n;\delta\nu_{excite})}{1 - P_e(\delta\nu_{excite};\delta\nu_{excite})P_e(\delta\nu_{excite} \pm \delta\nu_n;\delta\nu_{excite})} \quad (11)$$

and where f_e is the probability to find electrons at $\delta\nu_{excite}$ and N^{-1}_M is a factor normalizing the $S^n_M(\delta\nu_{excite})$'s for M=SE or dCE.

Similarly, the iCE-DNP lineshape can be calculated by taking into account all pairs of CE electrons and not just the ones that are directly affected by the MW irradiation:

$$S^n_{iCE}(\delta\nu_{excite}) = N^{-1}_{iCE}\sum_j f_j f_{j-}\frac{P_e(\delta\nu_j;\delta\nu_{excite}) - P_e(\delta\nu_j - \delta\nu_n;\delta\nu_{excite})}{1 - P_e(\delta\nu_j;\delta\nu_{excite})P_e(\delta\nu_j - \delta\nu_n;\delta\nu_{excite})} \quad (12)$$

where $\delta\nu_j$ is the frequency of the j bin of the EPR line, the relative intensities of the EPR line, f_j and f_{j-}, are the probabilities to find electrons at $\delta\nu_j$ and $\delta\nu_j - \delta\nu_n$, respectively, and N^{-1}_{iCE} is a factor that normalizes the $S^n_{iCE}(\delta\nu_e)$'s. The sum over j represents all pairs of electrons separated by $\delta\nu_n$ (all CE electron pairs) within the whole frequency range of the EPR spectrum.

As an example, the simulated normalized ^{1}H-SE-DNP, ^{13}C-SE-DNP, ^{13}C-dCE-DNP and ^{13}C-iCE-DNP lineshapes at 6.5 K are shown in Fig. 10. The SE-DNP shapes (magenta) look as expected, with positive and negative enhancement around $\mp\delta\nu_n$ from the center, respectively, for both the ^{1}H and ^{13}C nuclei. The ^{13}C-iCE-DNP shape (blue) is more complex and can be split into two parts: the main DNP effect, with positive and negative enhancement $\mp\frac{1}{2}\delta\nu_C$ from the center, and the additional DNP features with positive and negative enhancement $\delta\nu_H \mp \frac{1}{2}\nu_C$ and $-\delta\nu_H \mp \frac{1}{2}\delta\nu_C$ from the center. These additional DNP effects correspond to the proton shifted ^{13}C-CE (condition 4 and 4' in Fig. 3) mechanisms discussed for the four spin system $\{e_a - e_b - (^1\mathrm{H},^{13}\mathrm{C})\}$ in Section 3.2.2. The ^{13}C-dCE-DNP (green) and ^{13}C-iCE-DNP shapes are similar around the center of the main DNP effect, but the^{13}C-dCE-DNP is narrower

and does not show the proton shifted ^{13}C-CE.

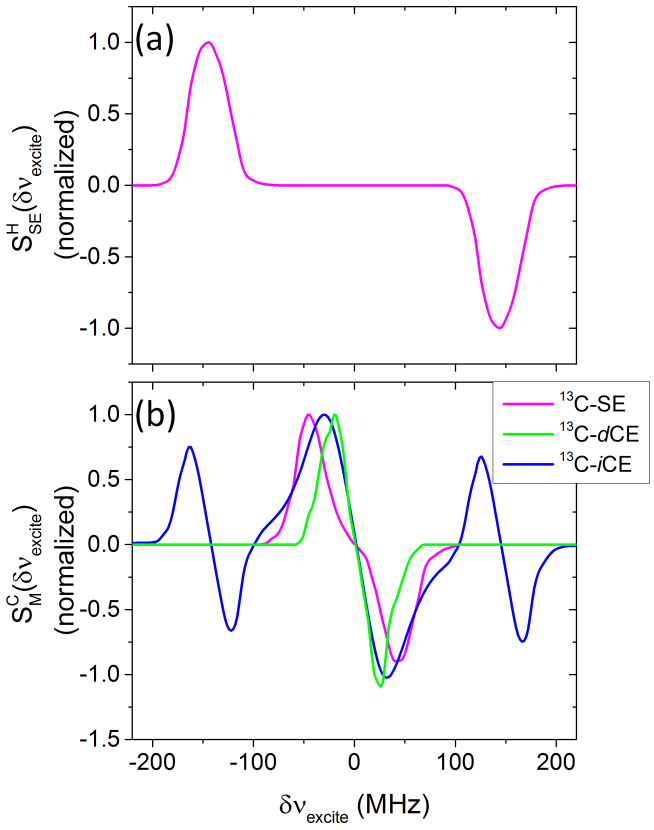

Figure 10: Simulated powder DNP spectra, $S^n_M(\delta\nu_e)$, where $n =^1$ H or ^{13}C and M=SE, dCE or iCE, used to fit the 6.5 K experimental DNP spectra: (a) the ^{1}H-SE (magenta) and (b) the ^{13}C-SE (magenta), the ^{13}C-dCE (green) and the ^{13}C-iCE (blue). The electron polarization used was simulated using the parameters given in Table 3. The MW frequency scale is given with respect to $\nu_{ref} = 94.863 \cdot 10^3$ MHz.

5.3 Results of the DNP analysis

The normalized experimental spectra can now be analyzed by fitting them to a linear combination of the normalized basic $S^n_C(\delta\nu_{excite})$, $S^n_{iCE}(\delta\nu_{excite})$ and $S^n_{CE}(\delta\nu_{excite})$ DNP spectra:

$$E_n(\delta\nu_{excite}) = k_{SE}S^n_{SE}(\delta\nu_{excite}) + k_{dCE}S^n_{dCE}(\delta\nu_{excite}) + k_{iCE}(S^n_{iCE}(\delta\nu_{excite}) - S^n_{iCE,0}) + c^n_{eq}, \quad (13)$$

where the c^n_{eq} is added to account for the thermal equilibrium value. The reason for the subtraction of the thermal equilibrium value $S^n_{iCE,0}$ from the iCE contribution is explained in Ref. [17]. We begin with fitting of the ^{13}C-DNP spectra shown in Fig. 7a. These fits are adjusted by eye and are shown in Fig. 11 (cyan line). For both temperatures the basic DNP shapes were calculated using the electron polarization obtained from the ELDOR analysis. From the compositions we see that the main part of the ^{13}C-DNP spectrum is a sum of ^{13}C-SE and ^{13}C-iCE contributions and that the extra features at $\pm$144 MHz result from the ^{13}C-iCE process through the proton shifted ^{13}C-CE. These extra features show the expected frequency separation between the positive and negative enhancements, ω_C, just as in the experiment. In order

to simplify the fitting procedure we decided to set $k_{dCE} = 0$. Moreover, the dCE contributing electrons are part of the sum in Eq. 12, which means that they were taken into account when calculating the basic iCE shape. However, it is important to note that in general the dCE and iCE enhancement contributions might be different because of different relaxation mechanisms involved. In the 6.5 K DNP spectrum we ignored the extra features caused by clustering or dimerization of the trityl radicals. The contributions of the SE and the iCE to the normalized ^{13}C-DNP are given in Table 3. Note that the sum $k_{SE} + k_{dCE} + k_{iCE}$ need not be equal to 1 because the SE, dCE and iCE shapes are normalized with respect to their maximums, which fall at different frequencies. The SE contribution, k_{SE}, is equal at both temperatures, while the iCE contribution, k_{iCE}, increases slightly at 6.5 K. The contribution of the iCE results in an overestimation of the intensities of the extra spectral features at 6.5 K, this could have been corrected if the dCE shape would have been taken into account.

In order to fit the^{1}H-DNP spectra shown in Fig. 7b, just the ^{1}H-SE-DNP mechanism was needed, as expected. The fits of the ^{1}H data are plotted in the SI.

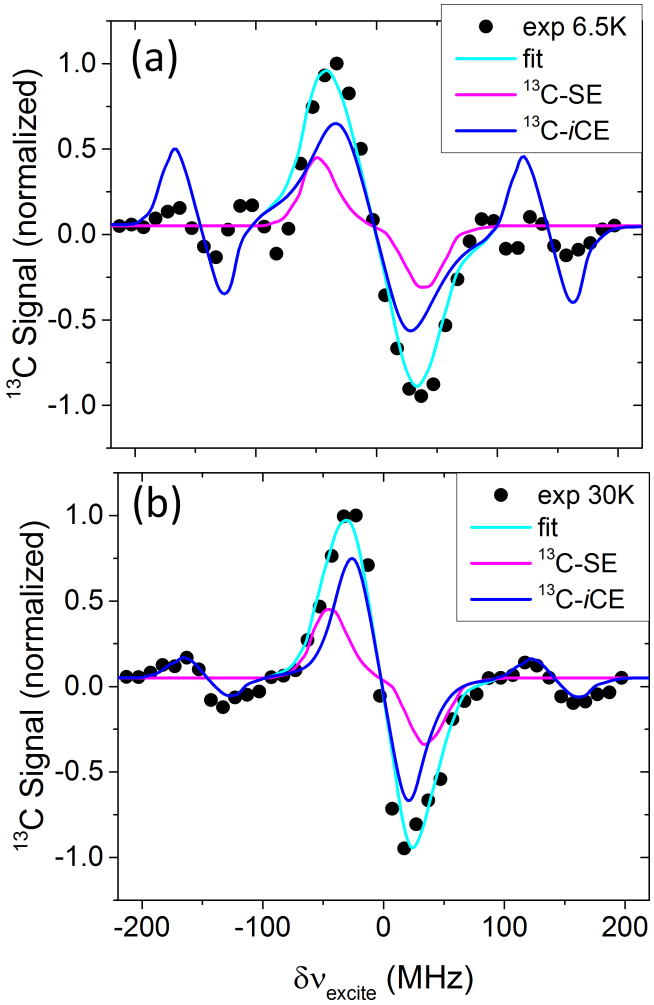

Figure 11: ^{13}C experimental DNP spectrum (symbols) measured at (a) 6.5 K and (b) 30K overlaid with the best fit (cyan). The components which make up the best fit: the SE (magenta) and the iCE (blue). The sum of these two shapes with the intensities as shown in the figure gives the fit (cyan). The MW frequency scale is given with respect to $\nu_{ref} = 94.863 \cdot 10^3$ MHz.

6 Discussion

In this work we discussed the DNP enhancements in systems containing two types of polarizable nuclei. DNP on heteronuclear spin systems often results in interesting phenomenon such as the polarization enhancement of one nucleus during MW irradiation at the "forbidden" transition frequencies of another nucleus [36, 37, 41, 45, 58, 59]. In an effort to explain these features we first examined the three spin system $\{^1\mathrm{H} - e - ^{13}\mathrm{C}\}$ and simulated DNP spectra using the "double-SE" mechanism, as described by de Boer [36, 37]. Subsequently, we moved on to examining the four spin system $\{e_a - e_b - (^1\mathrm{H}, ^{13}\mathrm{C})\}$. Inspection of the energy levels of this system revealed eight possible energy level degeneracies that result in the four standard ^{1}H and ^{13}C-CE conditions, (2,2',4,4'), with $|\omega_a - \omega_b| = \omega_n$ where $n = {}^1\mathrm{H}$ or $^{13}\mathrm{C}$, and the four "heteronuclear" CE conditions, (1,1',3,3'), with $|\omega_a - \omega_b| = \omega_H \pm \omega_C$.

At the standard^{13}C-CE conditions (4,4') we found that it is possible to obtain ^{13}C enhancements when irradiating on the DQ_{eH} and ZQ_{eH} transitions, corresponding to ^{1}H, an effect which we called the "proton-shifted ^{13}C-CE". This $\{^1$H-SE+^{13}C-CE$\}$ mechanism can also be extended to include the iCE mechanism when we consider large spin systems [17]. The DQ_{eH} and ZQ_{eH} transitions creates an electron polarization gradient over the EPR line and therefore causes a significant enhancement of the ^{13}C nuclei *via* the proton-shifted ^{13}C-iCE. The frequency separation between the positive and negative enhancements of the proton shifted ^{13}C-CE is ω_C.

At the "heteronuclear" CE conditions there is mixing of states involving both nuclei in the system, which results in possible cross talk between the nuclei. Subsequently, both nuclei are enhanced no matter which DQ_{en} or ZQ_{en} transition, with $n =^1$ H or ^{13}C, is irradiated. In addition, after polarization of both nuclei and saturation of one of them, the saturated nucleus recovers some of its polarization at the expense of the other nucleus.

Experimental ^{1}H-DNP and ^{13}C-DNP spectra were collected at 6.5 K and 30 K, on a sample containing 15 mM trityl in a glass forming solution of ^{13}C-glycerol/$\mathrm{H_2O}$. The ^{1}H-DNP spectrum could be attributed to the ^{1}H-SE mechanism, as expected. The ^{13}C-DNP spectrum showed the main DNP feature around the frequency position of the maximum of the EPR line, ω_e, and additional DNP features at $\sim \omega_e/2\pi \pm 95$ MHz and at the ^{1}H-SE-DNP frequencies, $\omega_e/2\pi \pm \omega_H/2\pi = \omega_e/2\pi \pm 144$ MHz. The frequency separation between the positive and negative enhancements of both features was ω_C. The inner features, at $\sim \omega_e/2\pi \pm 95$ MHz, decreased significantly after sonication of the sample, and were likely related to dimerization or clusters of trityl radicals. The analysis of the ^{13}C-DNP spectra was done using a sum of the basic ^{13}C-SE and ^{13}C-iCE lineshapes. The ^{13}C-iCE included the main DNP effect and the proton-shifted ^{13}C-iCE mechanism that was used to account for the outer features. As a function of temperature, we see that the SE contribution does not change while the iCE contribution increases slightly at 6.5 K. This is different from the analysis in our previous work where the SE was dominant at low temperatures, and there was a mixture of the SE and the dCE [54]. In this case the iCE contributes to the enhancement of what was previously thought to to be a SE contribution, this is because the iCE effectively includes the SE in it, through the electrons.

This analysis was possible after conducting ELDOR experiments, simulating them and then calculating the basic shapes of the SE and iCE from the simulated electron polarization distribution. Deviations between the experimental and simulated ^{13}C-DNP spectra could have possibly been corrected by introducing ^{13}C-dCE contributions. However, we decided to leave more accurate analysis for future work where time dependent features of the DNP lineshapes and their actual amplitudes will be investigated.

In this publication we have concentrated on defining the DNP effects appearing in small spin systems. In future studies these DNP effects must be extended to describe experimental observations of the cross-talk between the nuclei, reported in the literature, and usually attributed to Thermal Mixing (TM) [19, 37, 38, 56, 39, 40]. In order to do so, the enhancement mechanisms in model systems must be transferred to large spin systems with many electrons. This can be done, first, by extending the iCE-DNP mechanism, while taking into account observations that are derived from the TM description. To do so, further investigations of the heteronuclear high order CE conditions must be performed and their influence on the observed enhancements must be checked experimentally.

References

[1] C. Jefferies, Phys. Rev. 106, (1957), 164

[2] A. Abragam and M. Goldman, Reports on Progress in Physics 41 (1978), 395-467.

[3] T. J. Schmugge and C. D. Jeffries, Phys. Rev., 1965, 138, A1785.

[4] C.D. Jeffries, Dynamic Nuclear Orientation (Interscience, New York, 1963).

[5] A. Abragam and W. G. Proctor, Phys. Rev., 1958, 109, 1441.

[6] M. Borghini and A. Abragam, Compt. Rend., 1959, 203, 1803.

[7] O. S. Leifson and C. D. Jeffries, Phys. Rev., 1961, 122, 1781.

[8] R. A. Wind, M. J. Duijvestijn, C. van der Lugt, A. Manenschijn and J. Vriend, Prog. Nucl. Magn. Reson. Spectrosc., 1985, 17, 33-67.

[9] Y. Hovav, A. Feintuch and S. Vega, J. Chem. Phys., 2011, 134, 074509.

[10] T. Maly, G. T. Debelouchina, V. S. Bajaj, K. Hu, C. Joo, M. L. Mak-Jurkauskas, J. R. Sirigiri, P. C. A. van der Wel, J. Herzfeld, R. J. Temkin and R. G. Griffin, J. Chem. Phys., 2008, 128, 052211.

[11] C. F. Hwang and D. A. Hill, Phys. Rev. Lett. 18,(1967), 110

[12] C. F. Hwang and D. A. Hill, Phys. Rev. Lett. 19,(1967), 1011

[13] D. S. Wollan, Phys.Rev.B, 1976, 13, 3671-3685.

[14] A. V. Kessenikh, V. I. Lushchikov, A. A. Manenkov, Y. V. Taran, Sov. Phys. Solid State, 1963, 5, 321−329.

[15] A. V. Kessenikh, A. A. Manenkov, G. I. Pyatnitskii, Sov. Phys. Solid State, 1964, 6, 641–643.

[16] Y. Hovav, A. Feintuch and S. Vega, Journal of Magnetic Resonance, 2012, 214, 29-41.

[17] Y. Hovav, D. Shimon, I. Kaminker, A. Feintuch, D. Goldfarb and S. Vega, Phys. Chem. Chem. Phys., 2015, 17, 6053-6065.

[18] A. Abragam and M. Borghini, Progress in Low Temperature Physics (North-Holland, Amsterdam, 1964), Vol. 4.

[19] M. Borghini and K. Scheffler, Phys. Rev. Lett., 1971, 26, 1362-1365.

[20] V. A. Atsarkin, Soviet Journal of Experimental and Theoretical Physics, 1971, 32, 421.

[21] A. G. Redfield, Phys. Rev., 1955, 98, 1787-1809.

[22] B. N. Provotorov, Soviet Phys. JETP, 1962, 14, 1126-1131.

[23] A. Abragam, Principles of Nuclear Magnetism (Clarendon Press, Oxford, 1961).

[24] V. A. Atsarkin and A. V. Kessenikh, Applied Magnetic Resonance, 2012, 43, 7-19.

[25] A. W. Overhauser, Phys. Rev., 1953, 92, 411.

[26] T. R. Carver and C. P. Slichter, Phys. Rev., 1953, 92, 212.

[27] A. Abragam, Overhauser Effect in Nonmetals, Phys. Rev., 1955, 98, 1729-1735.

[28] L. H. Bennett and H. C. Torrey, Phys. Rev., 1957, 108, 499.

[29] T. Can, M. Caporini, F. Mentink-Vigier, B. Corzilius, J. Walish, M. Rosay, W. Maas, M. Baldus, S. Vega and T. Swager, J. Chem. Phys., 2014, 141, 064202.

[30] K. H. Hausser and D. Stehlik, Dynamic Nuclear Polarization in Liquids, Adv. Magn. Opt. Reson., 1968, 3, 79-139.

[31] V. Denysenkov, M. J. Prandolini, M. Gafurov, D. Sezer, B. Endeward and T. F. Prisner, Liquid state DNP using a 260 GHz high power gyrotron, Phys. Chem. Chem. Phys., 2010, 12, 5786-5790.

[32] M. Gafurov, V. Denysenkov, M. J. Prandolini and T. F. Prisner, Temperature Dependence of the Proton Overhauser DNP Enhancements on Aqueous Solutions of Fremy's Salt Measured in a Magnetic Field of 9.2 T, Appl. Magn. Reson., 2012, 43, 119-128.

[33] P. Neugebauer, J. G. Krummenacker, V. P. Denysenkov, C. Helmling, C. Luchinat, G. Parigi and T. F. Prisner, High-field liquid state NMR hyperpolarization: A combined DNP/NMRD approach, Phys. Chem. Chem. Phys., 2014, 16, 18781-18787.

[34] Ü. Akbey, F. Camponeschi, B. van Rossum and H. Oschkinat, ChemPhysChem, 2011, 12, 2092-2096.

[35] O. Lafon, A. S. L. Thankamony, T. Kobayashi, D. Carnevale, V. Vitzthum, I. I. Slowing, K. Kandel, H. Vezin, J. Amoureux, G. Bodenhausen and M. Pruski, J. Phys. Chem. C, 2013, 117, 1375-1382.

[36] W. de Boer, J. Low Temp. Phys., 1976, 22, 185-212.

[37] W. de Boer, M. Borghini, K. Morimoto, T. O. Niinikoski and F. Udo, J. Low Temp. Phys., 1974, 15, 249-267.

[38] S. F. J. Cox and V. Bouffard and M. Goldman, Journal of Physics C: Solid State Physics, 1973, 6, L100.

[39] L. Lumata, A. K. Jindal, M. E. Merritt, C. R. Malloy, A. D. Sherry and Z. Kovacs, J. Am. Chem. Soc., 2011, 133, 8673-8680.

[40] L. Lumata, M. Merritt, C. Malloy, A. D. Sherry and Z. Kovacs, Applied Magnetic Resonance, 2012, 43, 69-79.

[41] I. J. Day, J. C. Mitchell, M. J. Snowden and A. L. Davis, Magn. Reson. Chem., 2007, 45, 1018-1021.

[42] F. Blanc, L. Sperrin, D. A. Jefferson, S. Pawsey, M. Rosay and C. P. Grey, J. Am. Chem. Soc., 2013, 135, 2975-2978.

[43] O. Lafon, M. Rosay, F. Aussenac, X. Lu, J. Trébosc, O. Cristini, C. Kinowski, N. Touati, H. Vezin and J. Amoureux, Angew. Chem. Int. Edit., 2011, 50, 8367-8370.

[44] O. Lafon, A. S. L. Thankamony, M. Rosay, F. Aussenac, X. Lu, J. Trebosc, V. Bout-Roumazeilles, H. Vezin and J. Amoureux, Chem. Commun., 2013, 49, 2864-2866.

[45] S. Reynolds and H. Patel, Appl. Magn. Reson., 2008, 34, 495-508.

[46] C. Song, K. Hu, C. Joo, T. M. Swager and R. G. Griffin, J. Am. Chem. Soc., 2006, 128, 11385-11390.

[47] Y. Matsuki, T. Maly, O. Ouari, H. Karoui, F. Le Moigne, E. Rizzato, S. Lyubenova, J. Herzfeld, T. Prisner, P. Tordo and R. G. Griffin, Angew. Chem. Int. Edit., 2009, 48, 4996-5000.

[48] C. Sauvée, M. Rosay, G. Casano, F. Aussenac, R. T. Weber, O. Ouari and P. Tordo, Angew. Chem. Int. Edit., 2013, 52, 10858-10861.

[49] D. Shimon, Y. Hovav, A. Feintuch, D. Goldfarb and S. Vega, Phys. Chem. Chem. Phys., 2012, 14, 5729-5743.

[50] D. Shimon, A. Feintuch, D. Goldfarb and S. Vega, Phys. Chem. Chem. Phys., 2014, 16, 6687-6699.

[51] J. H. Ardenkjær-Larsen, B. Fridlund, A. Gram, G. Hansson, L. Hansson, M. H. Lerche, R. Servin, M. Thaning and K. Golman, P.N.A.S, 2003, 100, 10158-10163.

[52] W. de Boer, M. Borghini, K. Morimoto, T. O. Niinikoski and F. Udo, J. Low Temp. Phys., 1974, 15, 249-267.

[53] W. de Boer, Dynamic orientation of nuclei at low temperatures, J. Low Temp. Phys., 1976, 22, 185-212.

[54] D. Banerjee, D. Shimon, A. Feintuch, S. Vega and D. Goldfarb, J. Magn. Reson., 2013, 230, 212-219.

[55] F. M. Vigier, D. Shimon, V. Mugnaini, J. Veciana, A. Feintuch, M. Pons, S. Vega and D. Goldfarb, Phys. Chem. Chem. Phys., 2014, 16, 19218-19228.

[56] F. Kurdzesau, B. van den Brandt, A. Comment, P. Hautle, S. Jannin, J. J. van der Klink and J. A. Konter, J. Phys. D-Appl. Phys., 2008, 41, 155506.

[57] S. Jannin, A. Comment and J. van der Klink, Applied Magnetic Resonance, 2012, 43, 59-68.

[58] J. H. Ardenkjaer-Larsen, S. Macholl and H. Jóhannesson, Applied Magnetic Resonance, 2008, 34, 509-522.

[59] K. J. Donovan, A. Lupulescu and L. Frydman, ChemPhysChem, 2014, 15, 436-443.

[60] Y. Hovav, I. Kaminker, D. Shimon, A. Feintuch, D. Goldfarb and S. Vega, PCCP, 2015, 17, 226-244.

[61] A. Feintuch, D. Shimon, Y. Hovav, D. Banerjee, I. Kaminker, Y. Lipkin, K. Zibzener, B. Epel, S. Vega and D. Goldfarb, J. Magn. Reson., 2011, 209, 136-141.

[62] D. Goldfarb, Y. Lipkin, A. Potapov, Y. Gorodetsky, B. Epel, A. M. Raitsimring, M. Radoul and I. Kaminker, J. Magn. Reson., 2008, 194, 8-15.

[63] Y. Hovav, A. Feintuch and S. Vega, J. Chem. Phys., 2011, 134, 074509.

[64] C. Cohen-Tannoudji, B. Diu, F. Laloë, Quantum Mechanics vols 1 and 2, (Paris: Wiley & Hermann 1977).

[65] C.P. Slichter, Principles of Magnetic Resonance, (Springer, Berlin Heidelberg, 1990).

[66] K. Hu, G. T. Debelouchina, A. A. Smith and R. G. Griffin, J. Chem. Phys., 2011, 134, 125105.

[67] I. Marin-Montesinos, J. C. Paniagua, M. Vilaseca, A. Urtizberea, F. Luis, M. Feliz, F. Lin, S. Van Doorslaer and M. Pons, Phys. Chem. Chem. Phys., 2015, 17, 5785-5794.